JGR Solid Earth

RESEARCH ARTICLE
10.1029/2022JB026191

The Effect of Shear Displacement and Wear on Fault Stability: Laboratory Constraints

Corentin Noël[1], Carolina Giorgetti[1], Marco M. Scuderi[1], Cristiano Collettini[1,2], and Chris Marone[1,3]

[1]Dipartimento di Scienze della Terra, La Sapienza Università di Roma, Rome, Italy, [2]Istituto Nazionale di Geofisica e Vulcanologia (INGV), Rome, Italy, [3]Department of Geosciences, Pennsylvania State University, University Park, PA, USA

Key Points:

- Laboratory investigation of fault stability with varying wear rate
- Shear displacement has a dominant impact on fault stability
- Independently of the fault wear rate, the rate-and-state stability parameters evolve continuously with shear displacement

Supporting Information:

Supporting Information may be found in the online version of this article.

Correspondence to:

C. Noël,
corentin.noel@uniroma1.it

Citation:

Noël, C., Giorgetti, C., Scuderi, M. M., Collettini, C., & Marone, C. (2023). The effect of shear displacement and wear on fault stability: Laboratory constraints. *Journal of Geophysical Research: Solid Earth*, *128*, e2022JB026191. https://doi.org/10.1029/2022JB026191

Received 5 DEC 2022
Accepted 16 MAR 2023

Author Contributions:

Conceptualization: Corentin Noël
Data curation: Corentin Noël
Formal analysis: Corentin Noël
Funding acquisition: Chris Marone
Investigation: Corentin Noël, Carolina Giorgetti
Methodology: Corentin Noël
Supervision: Cristiano Collettini, Chris Marone
Visualization: Corentin Noël
Writing – original draft: Corentin Noël
Writing – review & editing: Corentin Noël, Carolina Giorgetti, Marco M. Scuderi, Cristiano Collettini, Chris Marone

Abstract Faults are composed of a damage zone and a fault core with wear material that has accumulated during sliding. Fault zone width and structural complexity have been suggested as key factors that dictate the stability of fault slip and the transition from stable to unstable motion. Here we address the role of fault rock wear rate and the presence of gouge on the stability of frictional sliding. We performed biaxial shear experiments on quartz-rich bare rock surfaces having different resistances to abrasion (i.e., wear production with slip), as well as simulated quartz gouge. To characterize the influence of shear displacement on fault stability, constant velocity and velocity step experiments were performed to displacements up to 30 mm. Mechanical data are analyzed within the rate-and-state framework, and integrated with post-mortem microscopic analyses of the samples. For initially bare surfaces a shear displacement threshold is required to transition from stable to unstable sliding. Stick-slip events (laboratory earthquakes) evolve systematically as a function of fault slip. Shear displacement has a clear effect on the rate-and-state parameters (a-b) and D_c. For all our tests, (a-b) decreases with increasing shear displacement, implying enhanced velocity weakening and potential unstable behavior for larger fault slip. For high wear rates and simulated gouge, D_c decreases with increasing slip. However, for low wear rate faults, changes in D_c are negligible. Our results demonstrate that, fault stability varies systematically with fault slip and in particular that shear displacement and strain localization are dominant parameters controlling fault stability.

Plain Language Summary Large earthquakes mainly occur on faults having large cumulative slip. In the field, fault structure consists of a fault core made of wear product (rock flour) that is surrounded by fractured rocks (damage zone). Most of laboratory studies on fault stability, that is, the capability of fault to nucleate earthquake, consider faults either as only intact rock interfaces or wear product only. Here, we address the role of fault rock wear rate (wear development with slip) and the presence of fault gouge on the mode of frictional sliding (stable sliding vs. earthquake). Three fault systems were tested in the laboratory: intact rock surfaces having a low wear rate, intact rock surfaces having a high wear rate and wear product alone. We found that for all the tested faults, earthquake nucleation requires a certain amount of slip. Microstructural analyses of the fault after the experiment show that cumulative slip favors localization of the deformation necessary for earthquake nucleation. We show that the fault stability is not constant in time and space but depends on the fault history (cumulative displacement, shear localization, presence or absence of gouge).

1. Introduction

Large earthquakes mainly take place on faults that have accumulated large shear displacement (e.g., Manighetti et al., 2007; Scholz, 2019). For faults in the shallow crust, shear occurs within a zone of finite width that is composed of non-cohesive rock wear products, often referred to as gouge (Sibson, 1977). Fault gouge thickness increases with cumulative fault shear displacement (e.g., Hirose et al., 2012; Marrett & Allmendinger, 1990; Power et al., 1988; Scholz, 1987). Moreover, the accumulation of fault gouge tends to stabilize fault frictional motion (i.e., slip is accommodated through creep without large stress drop) (Byerlee, 1967; Engelder et al., 1975; Marone, 1998b; Marone et al., 1990; Tullis & Weeks, 1986; Wong et al., 1992). It has also been suggested that the frictional stability of felsic fault gouge varies as a function of shear displacement (Beeler et al., 1996; Biegel et al., 1989; Dieterich, 1981; Ikari et al., 2011; Marone, 1998b; Scuderi, Collettini, Viti, et al., 2017). The stability evolution is interpreted as a consequence of the degree of shear localization within the simulated fault gouge: the more the deformation is localized, the more the fault slip is unstable. This implies that for bare rock surfaces,

unstable behavior is expected as the deformations are forced to be localized at the interface between the two sheared surfaces (Beeler et al., 1996).

On natural faults that have undergone large shear displacement (or for faults having a high gouge production rate), a competition must take place between (a) localization of the deformation at the bare surface interfaces, (b) delocalization of deformation due to gouge production and wall rock brecciation, (c) fault zone lithification and frictional healing, and (d) shear localization within the gouge and wear material. The competition and interaction between these phenomena must take place during fault cumulative slip (Ben-Zion & Sammis, 2003; Sibson, 1986). In turn, this competition may influence the frictional stability of faults with increasing shear displacement, and thus, their potential seismic activity.

Experimental studies on fault stability generally consider the wall rock interface without gouge (e.g., Beeler et al., 1996; Blanpied et al., 1995; Fryer et al., 2022; Harbord et al., 2017; Marone & Cox, 1994; Marone et al., 1990), or simulated gouge alone (e.g., Biegel et al., 1989; Hadizadeh et al., 2015; Logan & Rauenzahn, 1987; Mair & Marone, 1999; Marone, 1998a, 1998b; Marone & Saffer, 2007; Rathbun & Marone, 2010). Only relatively few experimental studies have compared the stability difference between bare rock surface and gouge (Carpenter et al., 2014; Giacomel et al., 2021; Tesei et al., 2014), or have constrained the effect of shear displacement on fault stability during the natural development of a gouge layer with increasing shear displacement (e.g., Byerlee, 1967; Engelder et al., 1975; Scholz et al., 1972). Additionally, no systematic experimental studies have aimed at a better understanding of the influence of shear displacement on fault stability considering faults having differing wear rates and wear behaviors.

In this study, we aim to better characterize how fault stability evolves with shear displacement. Particularly, how fault gouge development affects fault stability. To this end, we performed experiments to cumulative slip ranging from 1 to 30 mm, on a suite of faults having different wear rates. During the experiments, the rate-and-state stability parameters of the fault are measured to understand how the development of gouge structure (or its non-development) affects fault stability.

2. Experimental Methods

2.1. Starting Samples

To infer how wear and wear rate affect fault stability, two initially intact rocks were chosen as starting material: a high porosity Fontainebleau sandstone (FS) and a low porosity quartzite. These samples were chosen as they present very different resistances to abrasion (i.e., wear production with slip) for the same initial mineral composition (>95% quartz). In high porosity FS, the grains are poorly cemented and wear production is enhanced. Additionally, simulated quartz gouge was also tested.

The quartzite comes from India and is often referred to as "Gaja Gray." XRD analysis shows that the sample is composed of 95.2% quartz, 2.4% muscovite and 2.4% chlorite. Optical microscopic analyses reveal that the initial grain size of the sample is mainly ranging from 75 to 125 μm diameter (see Figure S1 in Supporting Information S1). Before each mechanical test, the sample porosity was measured from the dry sample density (i.e., assuming a 100% quartz composition) and found to be 1.4 ± 0.2%. Gaja Gray quartzite was chosen because it is homogeneous at the sample scale and has a high resistance to abrasion.

Fontainebleau sandstone (FS) (south of Paris, France) is a quartz arenite made of almost 100% randomly oriented quartz grains (200- to 300-μm diameter) cemented by quartz cement. At the scale of a block (multi-decimeter), it is homogeneous, isotropic and has reproducible mechanical (e.g., Bied et al., 2002; Haied & Kondo, 1997; Noël, Pimienta, & Violay, 2019; Reviron et al., 2009; Schubnel et al., 2007; Sulem & Ouffroukh, 2006) and frictional (Noël, Passelègue, et al., 2019) properties. The sample porosity was measured from the dry sample density and found to be 18.5 ± 1%. Fontainebleau sandstone was chosen because it is homogeneous at the sample scale and has a low resistance to abrasion.

For the simulated gouge experiments, FS was ground and sieved to ensure an initial grain diameter lower than 63 μm. Laser granulometry analysis revealed that the 87% of the grains range from 0.49 to 62 μm with a median at 15.8 μm. Note that 30% of the grains have a diameter ranging from 16 to 44 μm (see Figure S1 in Supporting Information S1).

For the bare rock surface experiments (i.e., for quartzite and FS samples), two rectangular cuboids of 80 × 40 × 13 mm and 40 × 40 × 13 mm (±100 μm) were prepared for each experiment. The sliding surfaces were

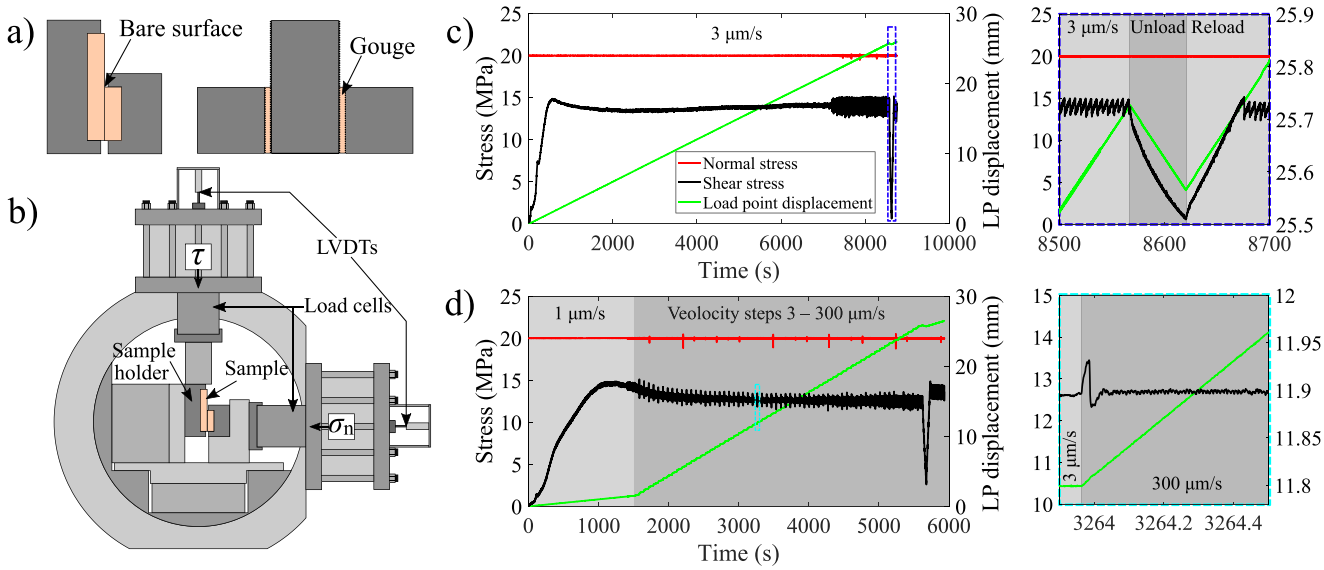

Figure 1. (a) Single direct and double direct shear configuration used for bare-surfaces and simulated-gouge experiments, respectively. (b) Biaxial apparatus used for the experiments. Horizontal and vertical pistons apply fault normal stress (σ_n) and shear stress (τ), respectively. Displacements are measured by Linear Variable Differential Transformers. Load cells measure applied forces close to the sample. (c) Data for one complete experiment at constant loading velocity. Blue dashed box is a zoom (at right) on the unload—reload cycle performed at the end of the experiment. (d) Data for one complete experiment with velocity step (here 3–300 μm/s). Light blue dashed box at center shows a zoom (at right) of a velocity step.

polished with #80 SiC sandpaper. Note that for FS, the surfaces roughness was mostly controlled by the grain size and porosity, because it is weakly cemented and polishing removes grains. For simulated gouge experiments, gouge layers were built on the sample holder (Figure 1a) using a precision level jig to obtain a uniform and reproducible sample with a layer thickness of 3 mm over the 50 × 50 mm sample holder.

2.2. Experimental Setup and Procedure

2.2.1. Apparatus

The experiments were performed using a biaxial deformation apparatus (BRAVA, Collettini et al., 2014). A horizontal (i.e., normal to the simulated fault) and a vertical (i.e., parallel to the shear direction) piston apply normal and shear forces to the fault, respectively. Forces are measured by load cells mounted close to the sample with a resolution of 0.15 kN and converted to stress. The horizontal and vertical displacements are measured by Linear Variable Differential Transformers mounted directly on the loading pistons with a resolution of 1 μm.

We used a single-direct shear configuration (SDS) for bare surface experiments and a double direct shear configuration (DDS) for simulated gouge experiments (Figure 1a). For the bare-surfaces experiments (SDS configuration), the larger rock sample is sheared against the stationary smaller rock sample. To ensure that we measured only rock friction (Figure 1b), a frictionless bearing surface was used ($\mu \ll 0.01$; Tesei et al., 2017), consisting of mirror polished steel surfaces lubricated with molybdenum grease (SAF-T-EZE Moly-Grade Anti-Seize from SAF-T-LOK©). For simulated-gouge experiments (DDS configuration), the central block is driven vertically between the stationary side blocks. Shear deformation in the simulated gouge layers was ensured by grooves in the surfaces of each forcing block. These grooves are oriented perpendicular to the shear direction and have a height of 0.8 mm and a spacing of 2 mm.

2.2.2. Sample Deformation

Before each experiment, the samples were oven dried at 60°C for 10 hr and cooled to room temperature for 2 hr. All the experiments were performed under room temperature and humidity conditions (Table 1). For FS bare surface experiments, two types of experiment were performed: (a) constant velocity experiments (Figure 1c), and (b) velocity step experiments (Figure 1d). For quartzite bare surfaces and simulated quartz gouge experiments, only velocity step experiments were performed.

Table 1
Summary of the Experimental Conditions

Experiment	Sample	Experiment type	Conditions
b1089	Fontainebleau sandstone	Constant velocity	3 μm/s
b1094			30 μm/s
b1096			100 μm/s
b1134	Fontainebleau sandstone	Velocity step	3–30 μm/s
b1114			3–100 μm/s
b1124			3–300 μm/s
b1113			3–100 μm/s
b1122	Fontainebleau sandstone	Stiffness evolution	3 μm/s
b1179	Quartzite	Velocity step	3–30 μm/s
b1178			3–100 μm/s
b1180			3–300 μm/s
b1145	Quartz gouge	Velocity step	3–30 μm/s
b1143			3–100 μm/s
b1144			3–300 μm/s

Note. All the experiments were performed at a normal stress of 20 MPa and under room temperature (26°C) and humidity (~27% for Fontainebleau sandstone experiments, ~89% for quartzite experiments, and ~50% for quartz gouge experiments).

For the constant velocity experiments (Figure 1c), after placing the samples into the apparatus, the normal stress (σ_n) was raised slowly in steps of 0.5 MPa up to 20 MPa. The vertical piston was then advanced at 1 μm/s until the vertical load reached about 1 kN ($\sigma_n \approx 0.6$ MPa), after which the load point velocity was set to 3, 30 or 100 μm/s. The samples were then sheared at constant velocity for 25–27 mm (Figure 1c). Finally, an unload-reload cycle was performed to remeasure the effective loading stiffness (see zoom on Figure 1c), and the sample was allowed to slide for few more millimeters. For these experiments, the recording rate varied from 10 to 1,000 Hz depending on both the sliding velocity and the observed mechanical behavior.

For the velocity step experiments, the normal stress was raised in the same way until the target of 20 MPa was reached. Note that, for simulated gouge experiments, after the application of the normal stress, the sample was allowed to compact to quasi-steady state compaction (typically about an hour). Then, the shear stress was increased by advancing the vertical piston at 1 μm/s for 1.5 mm. Subsequently, the velocity step sequence was initiated (Figure 1d). To characterize the influence of shear displacement on fault frictional stability, a single velocity step protocol was used in each experiment during which the loading rate was varied between: 3–30 μm/s, 3–100 μm/s or 3–300 μm/s. During the velocity step sequence, the load point velocity was changed every 0.2 mm of displacement. An additional 3–100 μm/s velocity step was performed for FS bare surfaces, for which the velocity was changed every 2 mm. After 25–30 mm of displacement, we performed an unload-reload cycle at 3 μm/s to measure effective loading stiffness, after which the sample was allowed to slide for few more millimeters. For these experiments, the recording rate was set to 10 Hz during the initial shearing at 1 μm/s, and then increased to 1,000 Hz during the velocity steps.

2.2.3. Data Analysis

The normal stress and shear stress applied on the fault were computed as the ratio of the normal (horizontal) force and shear (vertical) force, respectively to the sample apparent contact area ($\sigma_n = F_n/A$ and $\tau = F_s/A$). The friction (μ) was computed as the ratio of shear to normal stress ($\mu = \tau/\sigma_n$).

From the velocity step experiments, and for each velocity upstep, the friction evolution with slip was fitted using the rate-and-state formulation. In this framework, the frictional response of a fault depends on the instantaneous sliding velocity and a state variable that describes the gradual evolution of the sliding surfaces with slip as (Dieterich, 1978; Ruina, 1983):

$$\mu = \mu_0 + a \ln\left(\frac{V}{V_0}\right) + b \ln\left(\frac{V_0 \theta}{D_c}\right), \tag{1a}$$

where considering the so-called slip (or Ruina) law, the state variable θ evolution is:

$$\frac{d\theta}{dt} = -\frac{V\theta}{D_c} \ln\left(\frac{V\theta}{D_c}\right), \tag{1b}$$

with μ_0 being the friction at the reference velocity V_0 and V is the fault slip velocity. When the sliding velocity is increased from V_0 to V, friction first increases proportionally to the parameter a, the "direct effect," and then decays to a new steady-state value over a characteristic sliding distance D_c. The decay is proportional to the parameter b, the "evolution effect." In this formulation, if $(a\text{-}b)>0$, the fault exhibits a velocity strengthening behavior and is intrinsically stable. However, if $(a\text{-}b)<0$, the fault exhibits a velocity weakening behavior and might experience dynamic instability. To fit the experimental data, Equation 1 is coupled with a one-degree-of-freedom description of the elastic interaction between the frictional surface and the surrounding medium:

$$\frac{d\mu}{dt} = K(V_{LP} - V), \tag{2}$$

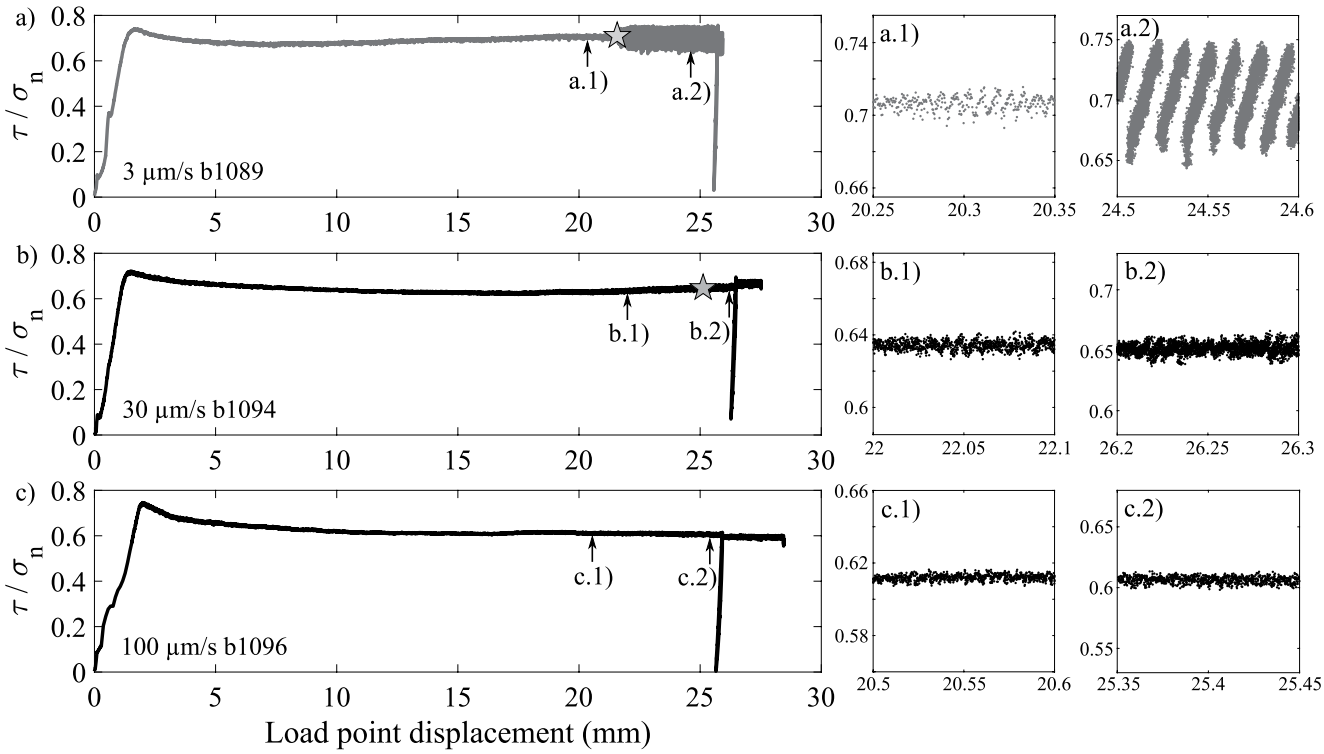

Figure 2. Friction response as a function of the load point displacement for the constant velocity experiments performed on Fontainebleau sandstone bare surfaces. (a) 3 µm/s. (b) 30 µm/s. (c) 300 µm/s. The stars on panel (a and b) represent the first stress drop higher than 0.5 MPa. Zooms of the curves are presented in panels on the right and show the spectrum of mechanical behavior with larger stress drops for lower shear velocities. Note that for the panels (a–c), the *x*- and *y*-axis have the same scale. Also, for the panels at right, the relative scales of the *x*- and *y*-axes are the same.

where, t is time, K is the loading stiffness and V_{LP} is the load point velocity. We inverted the experimental data for stable velocity steps using the software package developed by Skarbek and Savage (2019).

The loading stiffness was measured from the unload-reload cycle at the end of each experiment (Figure 1b). Only the initial, linear section of the shear stress curves were used to compute stiffness K. Additionally, we performed an experiment dedicated to measuring stiffness evolution under similar conditions (Table 1). During this experiment, regular cycles of unloading–reloading were conducted, and K was computed using the linear sections of the reloading shear stress–load point displacement curve (see Figure S2 in Supporting Information S1).

3. Results

3.1. Constant Velocity Experiments

For the constant velocity experiments, and for all the load point velocities tested, the mechanical response of the FS bare surfaces (Figure 2) is similar for the first 15 mm of sliding. First, the friction shows a quasi-linear increase with the load point displacement. During this phase, the samples are assumed to behave elastically and the fault to be quasi-stationary. Note that the drops observed at a friction of about 0.1 and 0.3 are due to sample realignment within the forcing blocks. After this elastic phase, the fault starts to move and enters a non-linear strengthening phase up to a peak friction at 0.735 ± 0.014, which is reached between 1.1 and 1.45 mm of load point displacement. After the peak, the friction decreases slowly to a steady state, between 10 and 13 mm of displacement. At 15 mm of shear displacement, the average friction is 0.644 ± 0.043, considering all the sample tested, showing a very high degree of reproducibility. At larger load point displacement, the mechanical behavior depends on the load point velocity (Figure 2). For the experiment performed at 100 µm/s, friction remains constant, around the steady-state value, up to the end of the experiment. For the experiments performed at 3 and 30 µm/s, friction increases slightly, and small stress drops spontaneously arise (Figures 2a and 2b). With increasing shear displacement, the magnitude of the stress drops increases. For the experiment performed at 30 µm/s, the stress drops reach

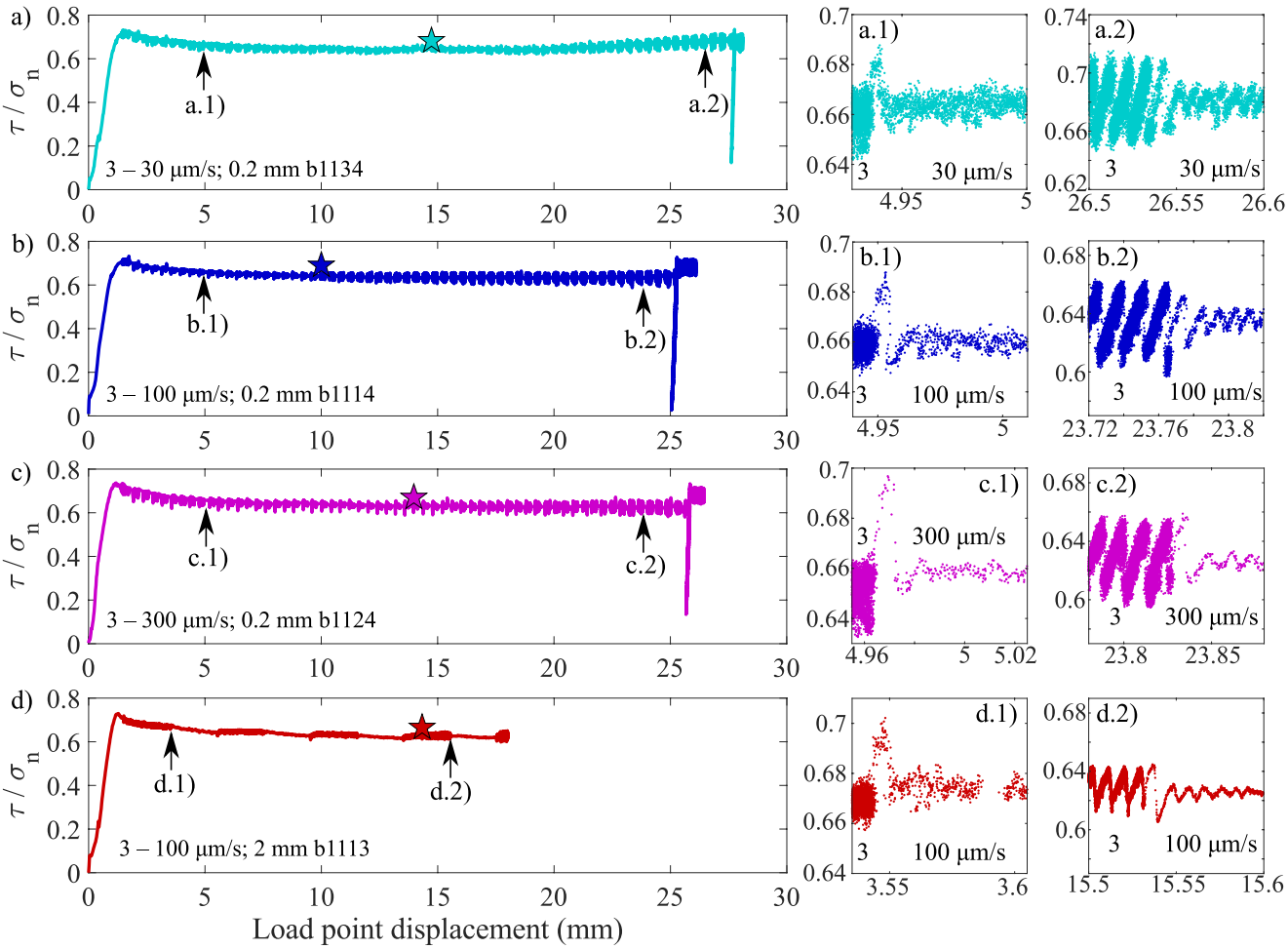

Figure 3. Friction response as a function of the load point displacement for the velocity step experiments performed on Fontainebleau sandstone bare surfaces. (a) 3–30 µm/s with velocity step every 0.2 mm of load point displacement. (b) 3–100 µm/s with velocity step every 0.2 mm of load point displacement. (c) 3–300 µm/s with velocity step every 0.2 mm of load point displacement. (d) 3–100 µm/s with velocity step every 2 mm of load point displacement. The stars represent the first stress drop higher than 0.5 MPa. Zooms of the curves are shown on the right for small and large load point displacements. Note that for the panels (a–c), the *x*- and *y*-axis have the same scale. Also, for the panels on the right, the relative scales of the *x*- and *y*-axes are the same.

a maximum value of 0.56 MPa at around 25 mm of displacement (Figure 2b). For the experiment performed at 3 µm/s, the stress drops grow up to a maximum of 2.2 MPa at 23 mm of shear displacement. Here, after about 22 mm of displacement, stress drops (ranging from 1 to 2 MPa) occur periodically (i.e., stick-slip behavior, Figure 2a).

In summary, the mechanical data obtained from the bare-surface experiments at constant velocity show that the transition from stable to unstable sliding, stick-slip occurrence, and the stress drop magnitude scale inversely with load point velocity. It is easier to nucleate instabilities at lower shear velocity (Figure 2).

3.2. Velocity Step Experiments

3.2.1. Mechanical Data

For the velocity step experiments performed on FS bare surfaces, the mechanical responses of the samples (Figure 3) are similar during the first 1.5 mm of load point displacement performed at a load point velocity of 1 µm/s. As for constant velocity experiments, the friction shows first a quasi-linear increase with load point displacement (elastic phase with a quasi-stationary fault). After the elastic phase, the fault starts to move and enters a strengthening phase up to a peak friction at 0.718 ± 0.011, reached between 1.1 and 1.45 mm of load point displacement. At 1.5 mm of displacement, the load point velocity was increased to 3 µm/s and the velocity step sequence starts. For all these experiments, the general trend of the friction–load point displacement curve

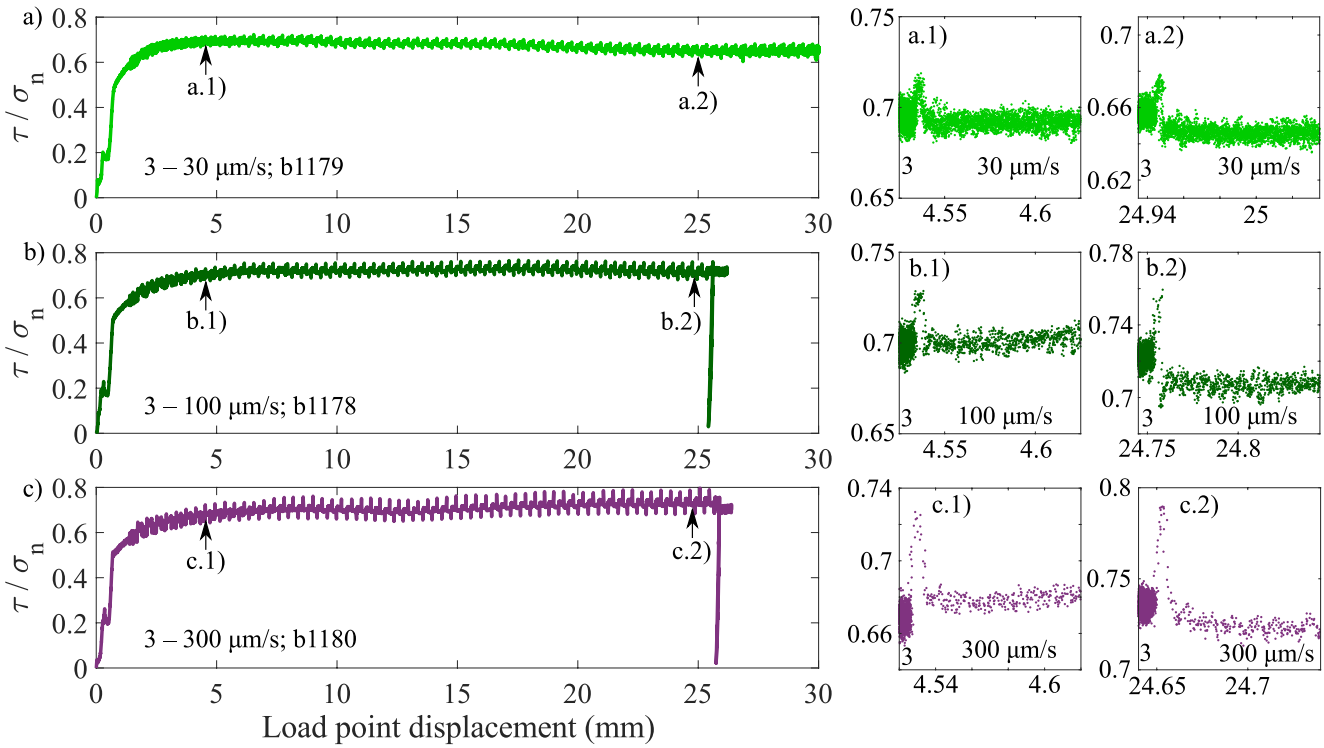

Figure 4. Friction response as a function of the load point displacement for the velocity step experiments performed on quartzite bare surfaces. (a) 3–30 µm/s. (b) 3–100 µm/s. (c) 3–300 µm/s. Zooms of the curves are shown on the right for small and large load point displacements. Note that for the panels (a–c), the *x*- and *y*-axis have the same scale. Also, for the panels on the right, the relative scales of the *x*- and *y*-axes are the same.

is similar to the constant velocity experiments (Figures 2 and 3): After the peak, the friction decreases slowly to a steady-state, reached between 10 and 13 mm of load point displacement. At 15 mm of load point displacement, the average friction is 0.637 ± 0.009 and remains around this value up to the end of the experiments. However, looking at individual velocity steps, the frictional behavior of the samples shows an evolution with shear displacement. At small displacement (Figures 3a.1–3d.1), the frictional behavior is stable and exhibits velocity neutral/strengthening behavior. At load point displacement between 10 and 15 mm, small stress drops (i.e., instabilities) initiate and grow with increasing strain. These stress drops eventually get bigger than 0.5 MPa (see stars on Figure 3) and continue growing to about 20–23 mm of load point displacement. At this large displacement, stress drops reach a constant magnitude (∼2 MPa). As has been observed for the constant velocity experiments, the experimental data show that the stress drop magnitude depends on the load point velocity: the higher the load point velocity the smaller the stress drop (Figure 3a.2–3d.2). Note that, while the constant velocity tests at 100 µm/s showed only stable sliding, without stick slip instabilities (Figure 2), here we find that stress drops occur at 30, 100, and 300 µm/s after stepping up to this velocity from 3 µm/s (Figure 3).

For the velocity step experiments performed on quartzite bare surfaces, the mechanical response of the samples (Figure 4) is similar during the first 1.5 mm of load point displacement, when the sample is sheared at a constant load point velocity of 1 µm/s. The friction shows first a quasi-linear increase with the load point displacement (elastic phase with a quasi-stationary fault). When the friction reaches 0.492 ± 0.017, the curve is no longer linear and fault sliding initiates. The fault then enters a strengthening phase and reaches a maximum friction of 0.696 ± 0.016 between 4.5 and 5 mm of displacement, after which, the average friction remains relatively constant (Figure 4). Looking at individual velocity steps, friction shows a characteristic evolution with velocity steps (see zooms in Figure 4). Indeed, directly after a velocity step, the friction increases instantaneously up to a peak (i.e., the direct effect) and then decays up to a new steady-state value (i.e., the evolution effect). Interestingly, at small load point displacement (Figures 4a.1–4c.1), velocity steps show velocity neutral or velocity strengthening behavior. However, as shear displacement increases (Figures 4a.2–4c.2), steady-state friction is lower for higher velocity (i.e., velocity weakening behavior). In general, the mechanical data show a gradual evolution from velocity neutral/strengthening to velocity weakening with increasing shear displacement (Figure 4).

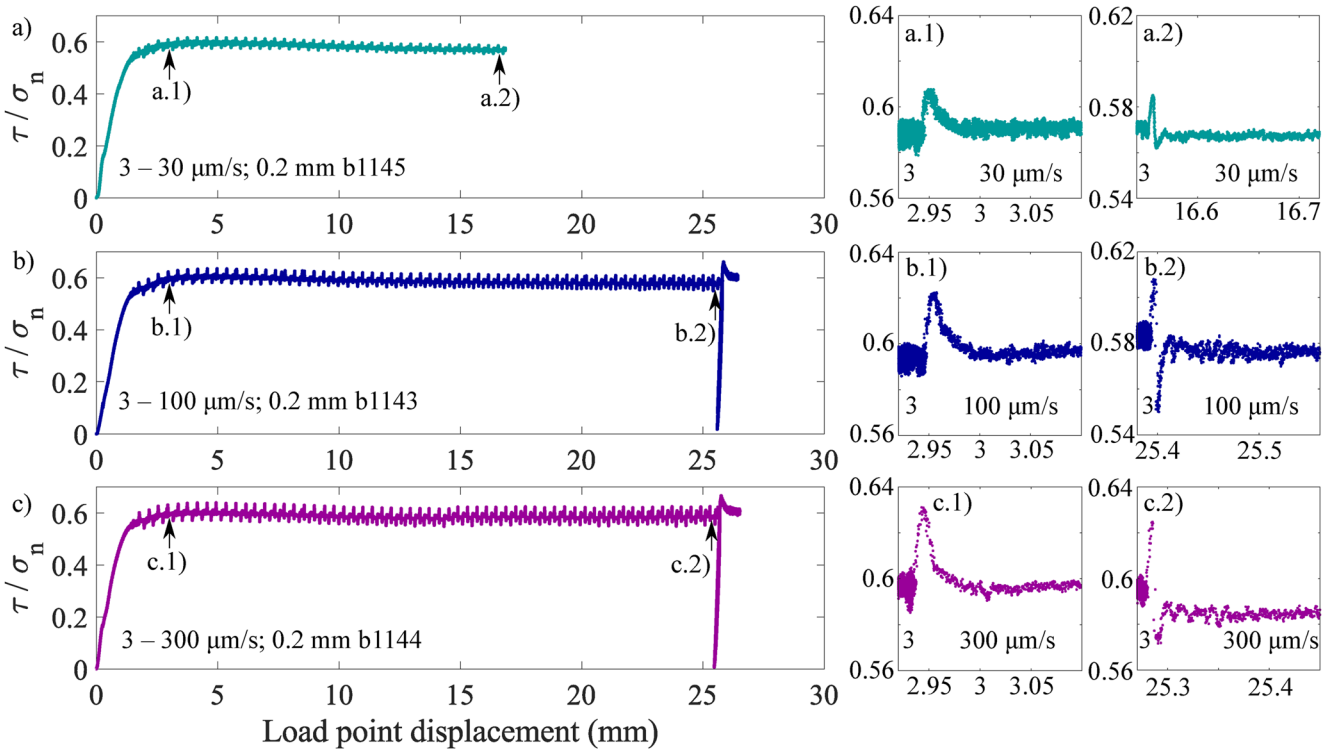

Figure 5. Friction response as a function of the load point displacement for the velocity step experiments performed on simulated gouge. (a) 3–30 µm/s. (b) 3–100 µm/s. (c) 3–300 µm/s. Zooms of the curves are shown on the right for small and large load point displacements. Note that for the panels (a–c), the *x*- and *y*-axis have the same scale. Also, for the panels on the right, the relative scales of the *x*- and *y*-axes are the same.

For the velocity step experiments performed on simulated quartz gouge, the mechanical response of the samples (Figure 5) is similar during the first 1.5 mm of load point displacement performed at a load point velocity of 1 µm/s. In the early loading stage, friction increases with load point displacement. This increase is not linear but shows a slight strengthening reduction (i.e., decreasing of slope) with increasing load point displacement, typical of double-direct shear experiments on simulated gouge. At 1.1–1.2 mm of displacement, the friction reaches 0.507 ± 0.004 and the strengthening behavior reduces. Eventually, friction reaches a maximum of 0.602 ± 0.004 at 4.4–4.6 mm of displacement. After the peak friction, the samples enter a slow weakening phase up to 12–14 mm of displacement after which a steady-state is reached. At 15 mm of load point displacement, the average friction is 0.578 ± 0.007 and remains around this value until the end of the experiments. Looking at individual velocity steps, friction evolves with a direct and an evolution effect as a consequence of the step (see zooms in Figure 5). Here again, the behavior evolves with increasing load point displacement: At small displacements (Figures 5a.1–5c.1), when the fault is subjected to a velocity step, and for all tested velocities, friction is velocity neutral or velocity strengthening. However, at large load point displacement (Figure 5a.2–5c.2), friction evolves to velocity weakening. Additionally, at large load point displacement, a friction decrease overshoot at the onset of the evolutionary effect is systematically observed.

3.2.2. Rate-And-State Stability Parameters

To better characterize the stability of the tested faults with shear displacement, we inverted the rate-and-state parameters for each velocity step performed. For each of our fault types, the rate-and-state stability parameters evolve systematically with shear displacement (Figures 6 and 7).

For quartzite (Figure 6a), (*a*-*b*) rapidly decreases during the first 10 mm of displacement, decreasing from values ranging from 1.9×10^{-4} to 2.4×10^{-3} (i.e., velocity strengthening) to values ranging from -5×10^{-3} to -2.2×10^{-3} (i.e., velocity weakening). After 10 mm of displacement, (*a*-*b*) keeps on decreasing to values ranging from -5.5×10^{-3} to -2.9×10^{-3} at 25 mm of displacement. This decrease of (*a*-*b*) seems to be controlled by the increase of *b* while *a* remains relatively constant for a given velocity (Figures 7a and 7b). Additionally, faster upstep velocities seems to favor higher (*a*-*b*) value (Figures 6a and 8a). This in turn, seems to be controlled by higher value of *a* at higher upstep velocities (Figure 7a). For this quartzite bare rock surfaces, D_c does not seem

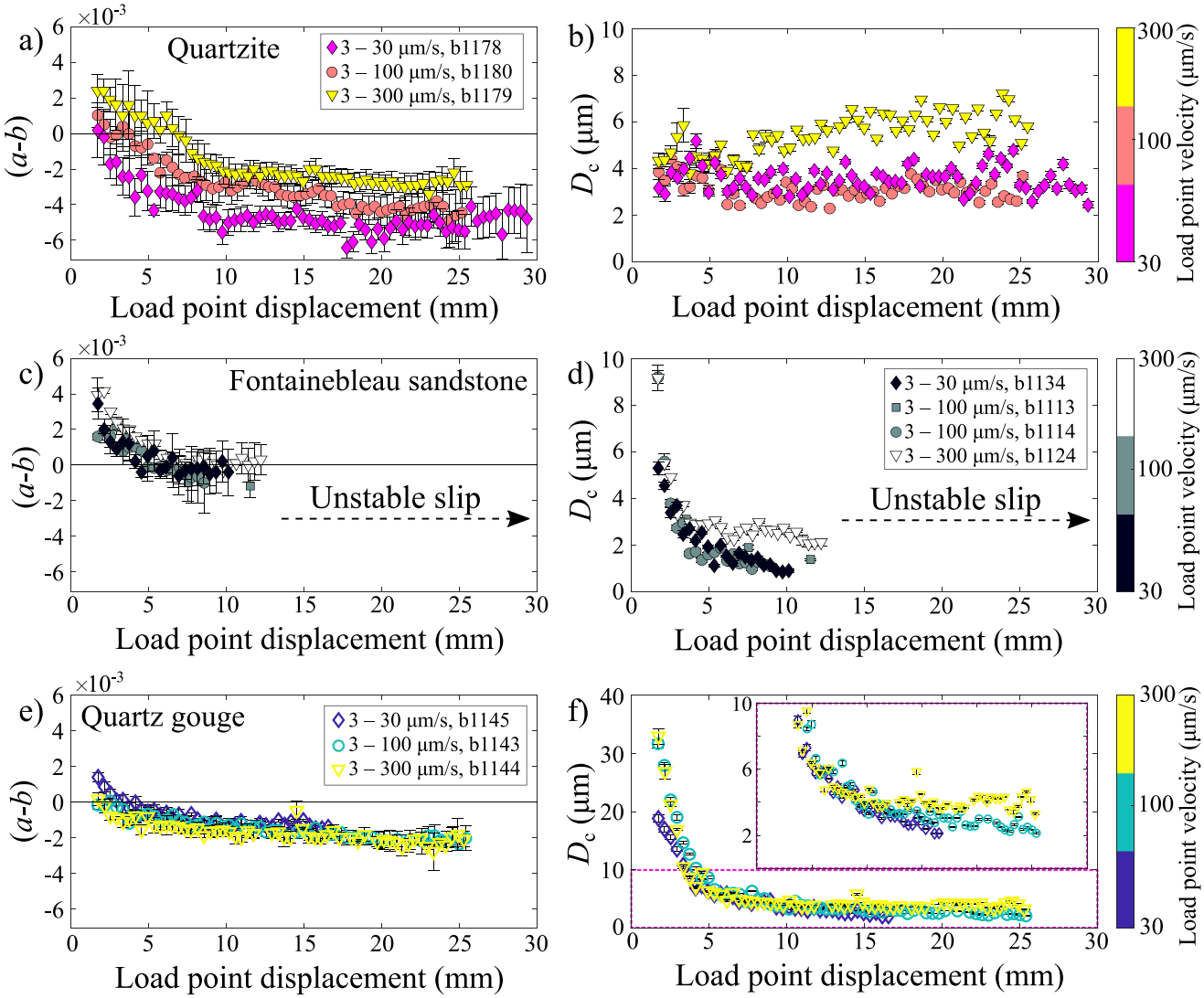

Figure 6. Inverted rate-and-state parameters (a-b) and D_c as a function of the load point displacement for: (a and b) quartzite, (c and d) Fontainebleau sandstone, and (e and f) simulated quartz gouge. The color represents the upstep velocity. Note that panels (a, c, and e) have the same x- and y-axis scale; as do panels (b, d) and the zoom of panel (f). The error bars show 95% confidence limits. Some raw data with their fit is available in the Supporting Information S1 Figure S5.

to be influenced by the shear displacement (Figure 6b). For 30 and 100 µm/s upstep velocity D_c ranges from 2 to 4.5 µm, while for 300 µm/s upstep velocity D_c ranges from 4 to 7 µm.

For FS (Figure 6c), (a-b) rapidly decreases during the first 5 mm of displacement, evolving from velocity strengthening to velocity neutral or weakening (i.e., from values ranging from 1.6×10^{-3} to 3.9×10^{-3}, to values ranging from -3×10^{-4} to 6×10^{-4}). After 5 mm of displacement, (a-b) keeps on decreasing to reach values ranging from -1.2×10^{-3} to -2×10^{-4} at 11 mm of displacement. After 11–12 mm of displacement, all samples exhibited unstable behavior, that is, (a-b) < 0. Here, the decrease of (a-b) also seems to be controlled by the increase of b while a remains relatively constant (Figures 7c and 7d), however, this is less pronounced than for the quartzite samples. Additionally, while at low shear displacement, no clear trend of (a-b) could be observe with increasing the upstep velocity (Figure 8c), at higher displacement, (a-b) slightly increases with the upstep velocity. For this sample, D_c is influenced by the shear displacement (Figure 6d). Indeed, D_c decreases from 9 to 2 µm within the first 5 mm of displacement. From 5 to 10 mm of shear displacement, D_c keeps on decreasing to reach 1.5 µm on average at 11 mm of shear displacement.

For simulated quartz gouge (Figure 6e), (a-b) rapidly decreases during the first 5 mm of displacement, passing from velocity neutral or strengthening to velocity weakening (i.e., from values ranging from -1.7×10^{-4} to

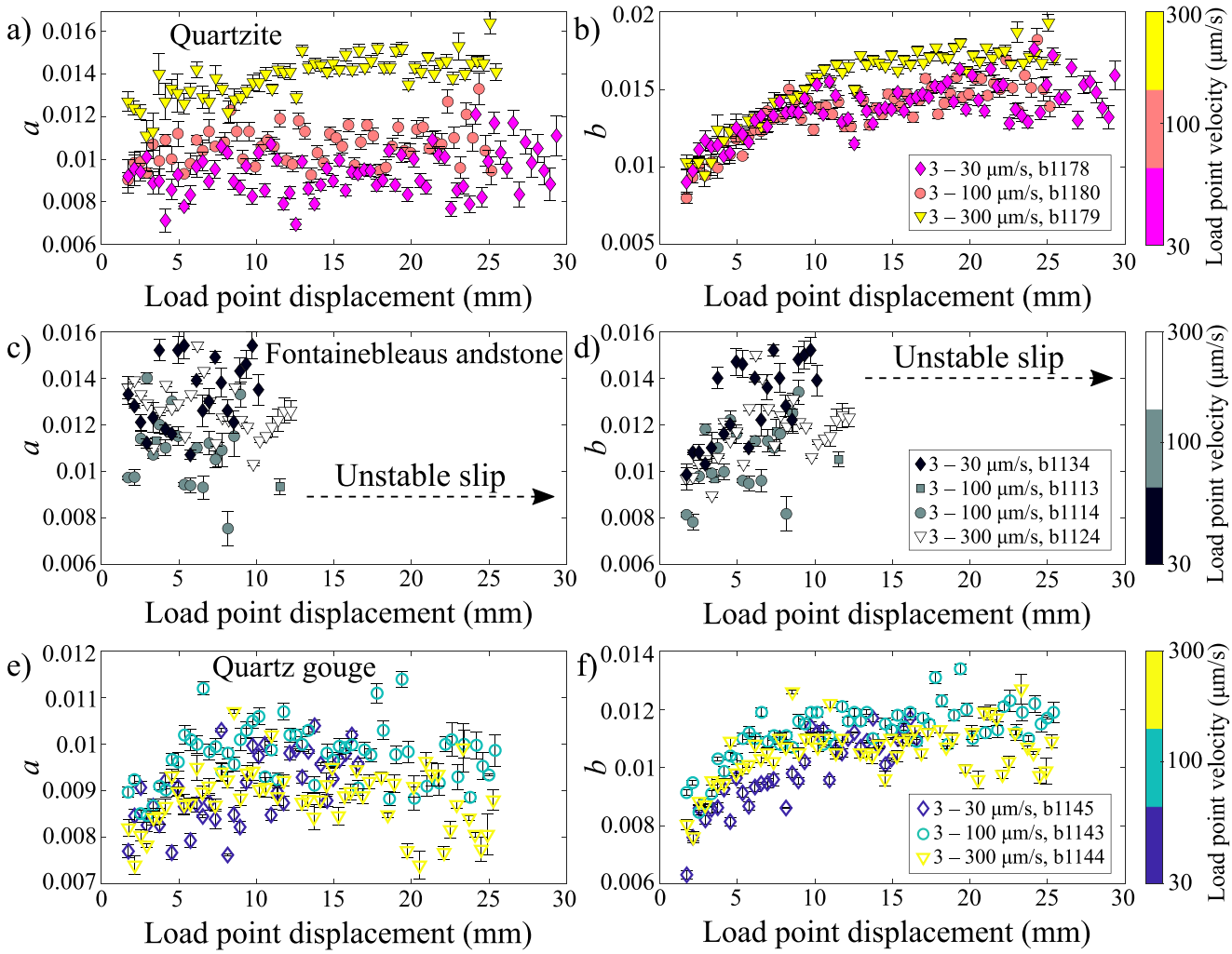

Figure 7. Inverted rate-and-state parameters *a* and *b* as a function of the load point displacement for: (a and b) quartzite, (c and d) Fontainebleau sandstone, and (e and f) simulated quartz gouge. The color represents the upstep velocity. The error bars show 95% confidence limits.

1.4×10^{-3} to values ranging from -4.7×10^{-4} to -1.3×10^{-3}). After 5 mm of displacement, (*a*-*b*) continues to decrease, reaching values ranging from -2.4×10^{-3} to -1.8×10^{-3} at 25 mm of displacement. Additionally, faster upstep velocities seem to favor lower (*a*-*b*) value (Figures 6e and 8e). In a similar fashion to the quartzite bare rock surfaces, (*a*-*b*) seems to be controlled by the parameter *b* that increases with displacement, while *a* remains essentially constant (Figures 7e and 7f). Interestingly, simulated quartz gouge shows the largest variation of D_c with shear displacement when compared to initially bare rock surfaces (Figure 6f). Indeed, D_c decreases from an average value of 27.8–7.5 μm in only 5 mm of shear displacement. After 5 mm of displacement, D_c keeps on decreasing to reach 2.7 μm on average at 25 mm of displacement.

In summary, for the three tested faults and independently of their wear behavior, (*a*-*b*) is largely influenced by the fault cumulative shear displacement, with second order variation induced by shear velocity (Figure 8). Particularly, the first 5–10 mm of displacement have a drastic impact on the velocity dependence of friction since all the tested faults transition from velocity strengthening (or neutral) to velocity weakening during this early stage. After this first phase, (*a*-*b*) keeps on decreasing with increasing displacement, without reaching a constant value even after 25 mm of displacement. Additionally, for FS and simulated quartz gouge, D_c follows the same trend as (*a*-*b*) with a large decrease within the first 5 mm, and a slower but continuous decrease during the rest of the experiments. For quartzite, D_c is initially much smaller than the other tested faults and remains constant with increasing shear displacement.

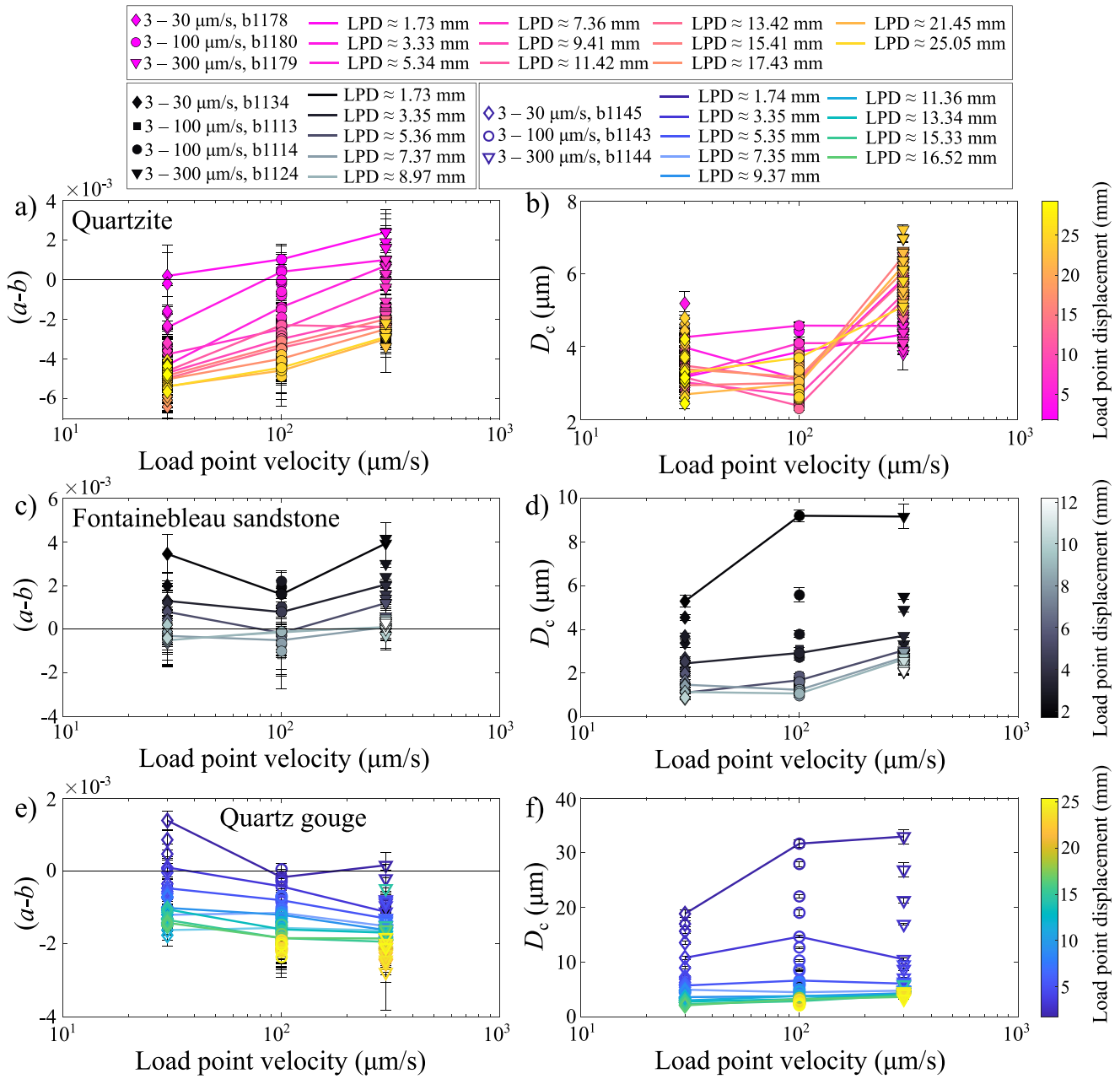

Figure 8. Inverted rate-and-state parameters (a-b) and D_c as a function of the load point velocity for: (a and b) quartzite, (c and d) Fontainebleau sandstone, and (e and f) simulated quartz gouge. The color represents the load point displacement. The lines connect points having similar load point displacements. The error bars show 95% confidence limits.

4. Post-Mortem Sample Analysis

After each experiment, the samples were extracted carefully from the sample holder and the fault surfaces were macroscopically inspected. For all the experiments performed on FS, the sliding surfaces are covered of a thin layer of gouge (see Figures S3 and S4 in Supporting Information S1). Interestingly, even fault sections that underwent small shear displacement (>~2 mm, i.e., right side of the large samples in Figures S3 and S4 in Supporting Information S1) were fully covered with wear materials. The FS samples recovered from the 3–30 and 3–300 µm/s velocity step experiments were epoxied and thin sections were prepared parallel to the slip direction at the center of the sample. Optical (Figure 9 and Figure S7 in Supporting Information S1) and scanning electron microscope analysis (Figures 10a–10d) revealed that, at the end of the experiments, the sample bare rock surfaces

were separated by a layer of 100- to 200-μm thick gouge. Note that the thickness of the produced gouge is typical of such surface at similar normal stress and total slip (e.g., Power et al., 1988; Scholz, 1987). Due to the experimental configuration, we were able to observe fault surfaces that experienced different amount of cumulative slip (Figure 9). For shear displacement smaller than 1 mm, only a small amount of wear materials were produced (Figure 9b). After about 2 mm of slip, wear materials is composed of relatively large grains (diameter <50 μm), and fills the porosity of the fault surface (Figure 9c). After about 3 mm of slip, the fault is covered with wear materials (Figure 9d). Here, both large grains (diameter <50 μm) and small grains are present. After about 12 mm of cumulative slip, the gouge is composed of only small grains (Figure 9e). With increasing fault cumulative displacement, wear production and comminution, lead to shear localization, which result in a reduction of the fault volume actively involved in shear deformation (i.e., localization of the deformations with increasing shear displacement). At the final stages, shear displacement was mainly accommodated on two boundary shear planes and Y-planes parallel to the shear direction (Figures 10a–10d). These shear planes are sometimes linked by R1 Riedel shear planes (Figure 10b). Additionally, the first rows of quartz grains in contact with the gouge show a high crack density (Figures 9f, 9g, 10a, and 10c). The crack density decreases with increasing distance from the wall rock: 2.5–4 mm away from the gouge, the crack density is close to that of the intact FS (i.e., permanent deformation close to null) (Figure 9). Interestingly, the stationary sides of the sample (top part in Figures 9, 10a, and 10c), show larger damage, than the non-stationary sides. This must arise as a consequence of the experimental configuration, as the stationary sides experience more cumulative slip when compared to the non-stationary side. Note that there are no major differences in both the macroscopic and microscopic structure when comparing the samples deformed under different experimental conditions (i.e., different velocity steps tested).

For the experiments performed on quartzite, a very limited amount of gouge could be observed on the 3–30 and 3–100 μm/s velocity steps experiment samples, and little gouge was produced (locally) during the 3–300 μm/s velocity step experiment (see Figure S4 in Supporting Information S1). Therefore, for quartzite samples it is assumed that, for the tested stresses and displacement boundary conditions, most of the shear deformation occurred at the interface between the bare rock surfaces.

For simulated quartz gouge, the samples were epoxied and studied under scanning electron microscope (Figures 10e and 10f). The analysis of the deformed samples revealed that the samples present a high density of relatively equally spaced R1 Riedel shear planes (every 100–200 μm). Additionally, two boundary shear planes of about 50 μm thickness, are highly developed as evidenced by high grain size reduction (Figure 10f). The higher grain size reduction in the boundary planes compared to the Riedel planes indicates that the majority of the deformation took place within the boundary planes. Note that, here again, no major difference in microscopical structure could be observed when comparing the different samples, regardless of the experimental conditions (i.e., different velocity steps tested).

5. Interpretation and Discussion

Our experimental results highlight that: (a) The emergence of unstable sliding requires a certain amount of shear displacement, and the stress drop magnitude depends on the load point velocity. (b) For all the sample tested, the rate-and-state stability parameter (a-b) decreases with increasing shear displacement. A strong decrease is observed at low shear displacement (from 0 to 10 mm) and a smaller but continuous decrease is measured at higher displacement (10–30 mm). (c) The decrease of (a-b) is a consequence of the increase of b parameter with increasing shear displacement. (d) For FS and simulated quartz gouge, D_c decreases with increasing shear displacement. As for (a-b), a strong decrease is observed at low shear displacement followed by a smaller but continuous decrease at higher displacement. For the quartzite bare surfaces, D_c remains relatively constant at all the shear displacements tested. (e) The sliding velocity has a smaller influence than shear displacement on (a-b) and D_c. For initially bare surfaces the friction rate-and-state parameter (a-b) slightly increases with the shearing velocity, while for gouge (a-b) decreases with increasing the velocity. For all the sample tested, larger shearing velocity seems to favor slightly higher D_c.

5.1. The Velocity Dependence of Stress Drop

Our experiments show larger stick-slip stress drops for lower sliding velocities and that sliding is only stable for the higher slip velocities. The control of sliding velocity on the stability transition is particularly apparent for the constant velocity experiments performed on FS. At large shear displacement, a transition from unstable sliding (i.e., stress drop) to stable sliding with increasing the load point velocity was observed (Figure 2). Additionally, both constant velocity and velocity step experiments showed that the maximum magnitude of the stress drops

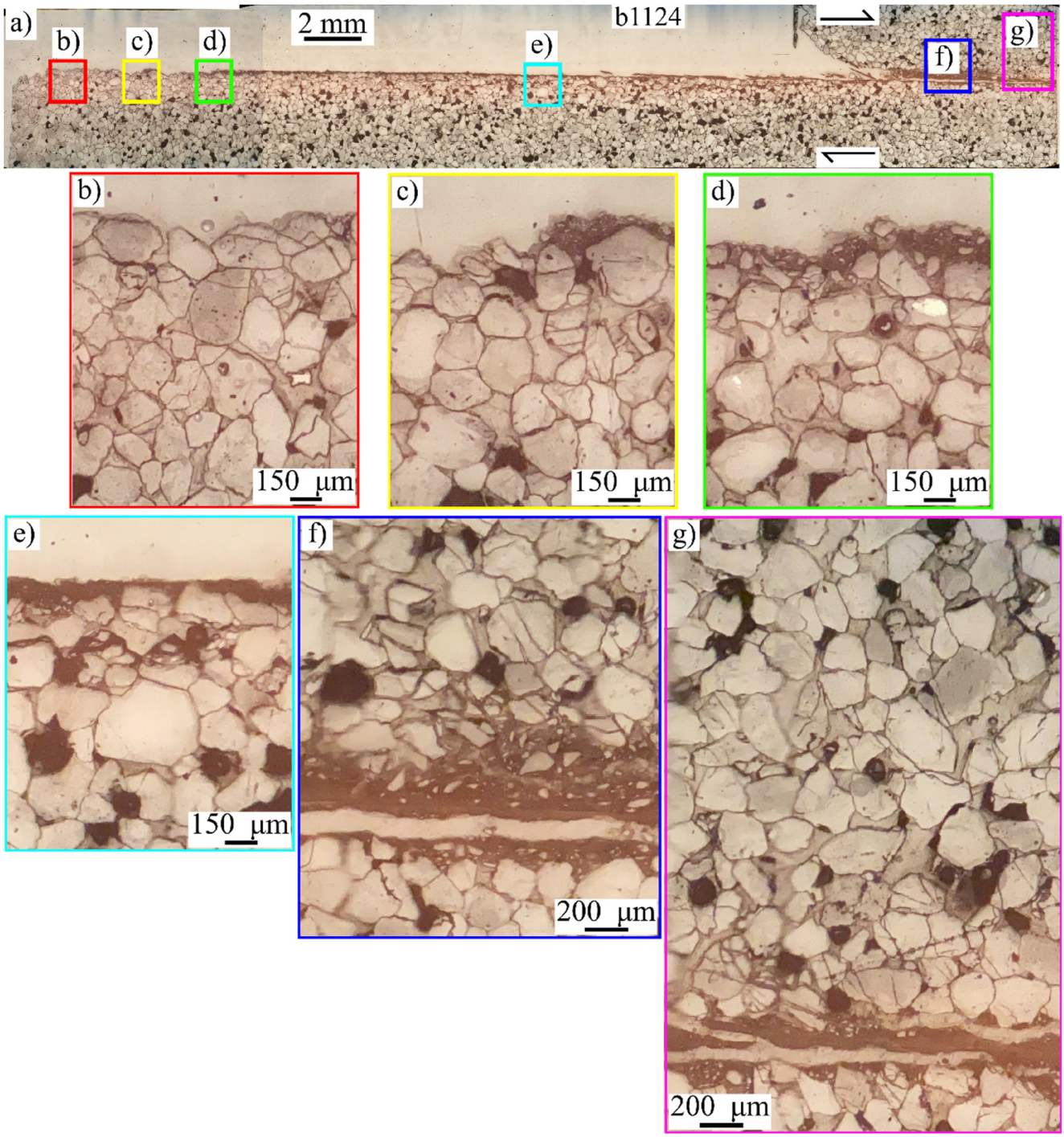

Figure 9. Post-mortem optical micrographs taken under polarized light of Fontainebleau sandstone deformed during the 3–300 µm/s velocity step experiment. (a) Mosaic of micrograph showing the fault section that has experienced different amount of slip. (b) Zoom on a section having experienced ∼1 mm of cumulative slip. Almost no wear products were formed here. (c) Zoom on a section having experienced ∼3 mm of cumulative slip. Wear materials (diameter <50 µm) mainly fill the fault porosity. (d) Zoom on a section having experienced ∼5 mm of cumulative slip. The fault is covered with wear materials of relatively large size (diameter <50 µm). (e) Zoom on a section having experienced ∼12 mm of cumulative slip. The fault is covered with fine wear materials of particle size too small to distinguish at this scale. (f) Zoom on a section having experienced ∼20 mm of cumulative slip. The fault is covered of very small grains and the first rows of quartz grains in contact with the gouge show a high crack density. (g) Zoom on a section having experienced ∼22 mm of cumulative slip showing that the crack density decreases with increasing distance from the wall rock.

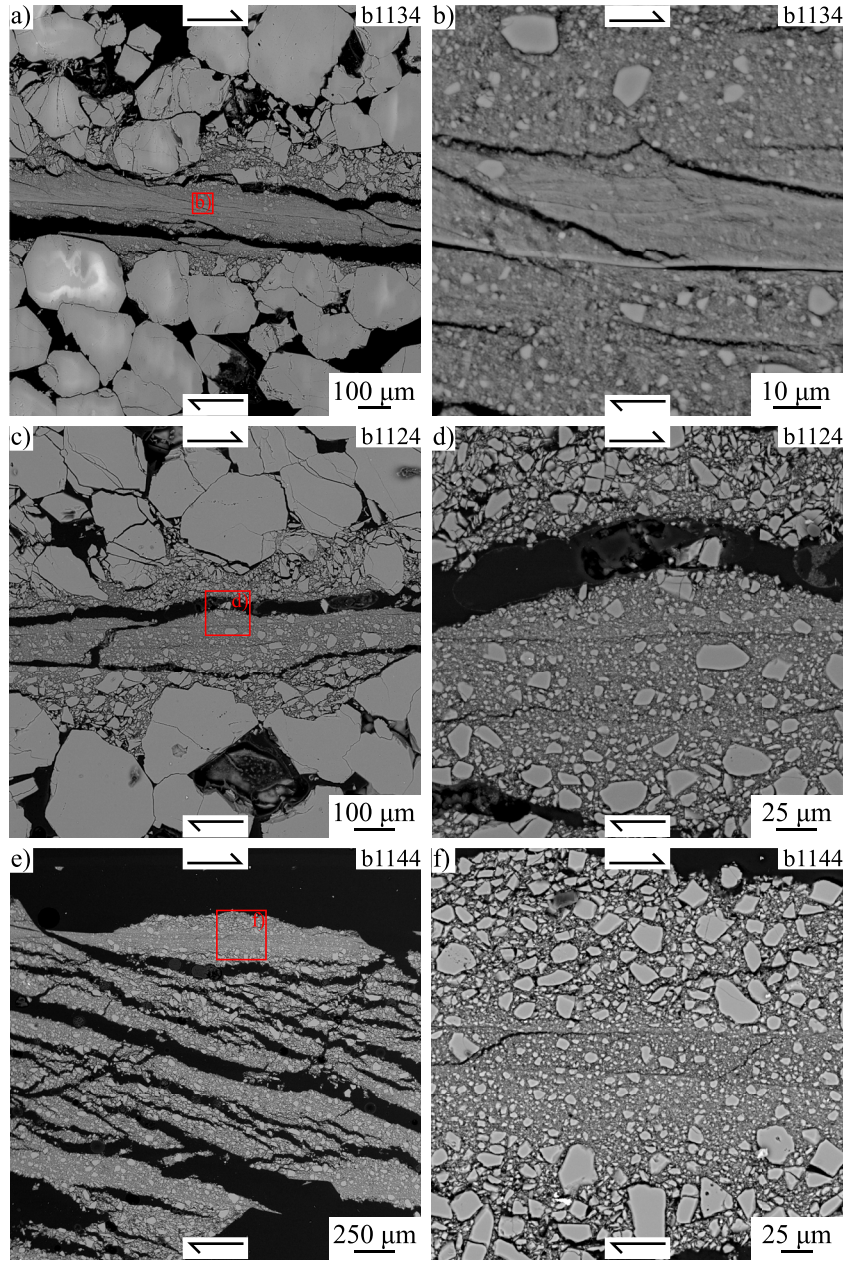

Figure 10. Post-mortem micrograph of samples obtain from scanning electron microscopy. (a) Micrograph of Fontainebleau sandstone (FS) deformed during the 3–30 μm/s velocity step experiment. The stationary side of the sample is at the top of the image. (b) Zoom indicated in (a) on Y- and Riedel shear planes. (c) Micrograph of FS deformed during the 3–300 μm/s velocity step experiment. The stationary side of the sample is at the top of the image. (d) Zoom indicated in (b) on Y-shear planes. (e) Micrograph of quartz gouge deformed during the 3–300 μm/s velocity step experiment. (f) Zoom indicated in (e) on boundary shear plane. The shearing direction is indicated by the arrow at the top and bottom of each micrograph.

depends on the load point velocity: the faster FS samples are sheared, the smaller the stress drops are (Figures 2 and 3). This reduction of the stress drop magnitude can be related to (a) the reduction of the maximum shear stress (just before the stress drop), and (b) the increase of the minimum shear stress (at the end of the stress drop) with increasing velocity (Karner & Marone, 2000). Such transition from unstable to stable sliding with increasing the velocity has been previously reported on quartz gouge (Leeman et al., 2016, 2018; Scuderi, Collettini, Viti, et al., 2017; Wong & Zhao, 1990), granite bare surfaces (Karner & Marone, 2000), quartzite bare surfaces and silica glass (Anthony & Marone, 2005; Beeler et al., 2014; Scuderi et al., 2014), PMMA (McLaskey et al., 2012), or paper (Baumberger et al., 1994; Heslot et al., 1994).

The scaling of stress drop with loading velocity has been interpreted as an effect of the reduction of healing time for frictional surfaces with increasing load point velocity (Beeler et al., 2014; He et al., 2003; Karner & Marone, 2000). Indeed, during the "stick" phase, prior to the instability, the fault is quasi-static, allowing for the real contact area of the fault to grow (Dieterich & Kilgore, 1994). Similarly to a slide-hold-slide experiments, for low load point velocity, the quasi-stationary phase lasts longer and the fault has more time to heal favoring an increase of the "static" friction (e.g., Beeler et al., 1994; Dieterich, 1972, 1978; Dieterich & Kilgore, 1994; Marone, 1998b).

If the healing time may explain the higher maximum shear stress (before the stress drop) at low velocity, the reduction of the shear stress after the stress drop must emerge from a combination of the fault system mechanical parameters linked to the slip history. Indeed, during a slip instability, the fault acceleration, deceleration, and arrest is related to a complex interaction between the velocity dependence of friction, the available elastic energy stored in the system, fault healing and the fault history. Taking as an example an oversimplified fault system, one can imagine that if the shear stress at the onset of stress drop is high, the elastic energy accumulated in the surrounding medium is also high. When the instability nucleates, the high level of energy favors higher acceleration and peak sliding velocity. As friction is sensitive to the sliding velocity (e.g., Dieterich & Conrad, 1984; Ruina, 1980, 1983), and particularly when approaching seismic slip velocity (e.g., Di Toro et al., 2004, 2011) this allows for a plethora of weakening mechanisms (e.g., Cornelio et al., 2022; Rice, 2006). Faster peak sliding velocity commonly involves (at least for felsic rocks) more frictional weakening, in turn allowing for larger stress drops. Such relationship between stress drop and loading velocity can be indirectly observed on natural earthquakes. Indeed, the stress drop of earthquakes has been shown to scale with the recurrence time of seismic event (that depends on the fault loading rate) (e.g., Kanamori & Allen, 1986; Marone et al., 1995).

5.2. Stability Evolution With Shear Displacement

5.2.1. (a-b) Evolution With Shear Displacement

For all the fault samples tested, independent of their wear behavior, the friction parameter (a-b) decreases with shear displacement. The reduction is largest during the first 5 or 10 mm of displacement and smaller afterward (Figure 6). Previous studies also reported variation of (a-b) with increasing shear displacements (Beeler et al., 1996; Biegel et al., 1989; Dieterich, 1981; Hadizadeh et al., 2015; Mair & Marone, 1999; Marone et al., 1990, 1992; Rathbun & Marone, 2010; Scuderi, Collettini, Viti, et al., 2017). Most of these experiments have been performed on simulated gouge (synthetic quartz or crushed Westerly granite) and are in agreement with our experiments, showing: first an important decrease of (a-b) within the first 4–7 mm of shear displacement, followed by a smoother decrease (Biegel et al., 1989; Dieterich, 1981; Scuderi, Collettini, Viti, et al., 2017). Beeler et al. (1996), sheared Westerly granite gouge up to 400 mm of displacement. They showed that (a-b) decreases during the first 50 mm of displacement, after which, it increases and stabilizes around velocity neutral value at around 150 mm of shear displacement. These authors also performed experiments on Westerly granite bare surfaces and measured a relatively constant velocity weakening friction dependence (i.e., (a-b) < 0) for 15–360 mm of shear displacement. Here, by performing a large amount of velocity steps at lower shear displacements, we observed that both intact rocks tested present a decrease of (a-b) with shear displacement. If this result could be expected for FS that produce a fairly large amount of gouge during sliding (Figures 9 and 10; Figures S3 and S4 in Supporting Information S1), and thus tends toward gouge-like behavior, this was not expected for quartzite, which produces very little to no gouge. Experimental data combined with microstructural analysis have shown that for gouge samples, the velocity dependence of friction is dependent on the microstructural accommodation of the strain (Beeler et al., 1996; Mair & Marone, 1999; Marone et al., 1990, 1992). If the deformation is distributed (e.g., bulk simple shear, wide deformation bands, multiple shear zones), the fault friction tends toward velocity strengthening behavior. However, if the deformation is localized (e.g., on a narrow shear band), the fault friction tends to be more velocity weakening. This transition from delocalized to localized deformation with increasing shear displacement has been well studied on gouge samples (e.g., Gu & Wong, 1994; Haines et al., 2013; Pozzi et al., 2022; Scuderi, Collettini, Viti, et al., 2017) and indeed shows a gradual localization of the deformation first on Riedel shear planes that coalesce to boundary or to boundary and Y-shear plans.

For our experiments, we relate the decrease of (a-b) observed for quartz gouge with increasing shear displacement to the localization of the deformation (Figure 9) on the boundary shear planes (Figure 10f). For FS, the decrease of (a-b) is likely to be related to the development of the gouge layer that promotes localization of deformation

along boundary and Y-shear planes (Figures 10a–10d). Finally, for our quartzite sample, assuming that (a-b) is only a function of the localization of the deformation, the reduction of (a-b) may come from the decapitation of small asperities, narrowing the volume involved in the deformation. Note that, polymineralic fault rocks may have a different wear production with slip when compared to pure quartz fault tested in this study. Indeed, the harness of the fault interface, that depends on the mineral content, influences the wear production with slip, in turn influencing fault stability transition (Wong et al., 1992).

5.2.2. D_c Evolution With Shear Displacement

For our experiments, for both simulated quartz gouge and FS bare surfaces, D_c decreases with increasing shear displacement, while for quartzite bare surface, D_c remains constant at all tested displacements (Figure 6). As for quartz gouge and FS bare surfaces, previous experimental studies performed on felsic simulated gouge show similar evolution of D_c with increasing shear displacement (Biegel et al., 1989; Dieterich, 1981; Marone & Kilgore, 1993; Scuderi, Collettini, Viti, et al., 2017). In the rate-and-state framework, D_c represents the sliding distance necessary for the fault surface to renew its contacts after a change in velocity (Rabinowicz, 1951). Therefore, it is often taken as a proxy for the average asperity size. Thus, for simulated gouge experiments, the decrease of D_c with increasing shear displacement is often interpreted as the comminution of the particle within the shearing zones (Dieterich, 1981; Sammis & Biegel, 1989; Scuderi, Collettini, Viti, et al., 2017). By performing experiments on simulated quartz gouge of different initial particle sizes and initial sample thicknesses, Marone and Kilgore (1993) demonstrated that D_c depends both on the shear band thickness and the particle sizes within the band. Decreasing the shear band thickness and the particle sizes reduces D_c. Here, D_c obtained on simulated quartz gouge at the end of the experiments scale with the thickness of the localized shear band observe in the microstructural analysis (Figure 10f). The same reasoning can be applied to bare surface experiments. For FS, the initial gouge formation causes a relatively large deformation zone that narrows when the strain starts to accumulate and localizes within the thin gouge layer produced. At the end of the experiments on FS, D_c is $\leq$2 μm, similar to the thickness of the localized shear zone observed in the microstructural analysis (Figures 10b and 10d). For quartzite, as the wear production is low, D_c is relatively constant as the deformation is forced to be localized at the interface between the two sliding walls. The limited wear products, resulting from the decapitation of the asperities, is not enough to cover the surface and significantly affect the thickness of the deforming zone and the average asperity size.

5.2.3. Nucleation of Instabilities With Shear Displacement

After fault reactivation (i.e., once fault slip has initiated), fault stability is often analyzed using the rate-and-state framework (Dieterich, 1978; Ruina, 1983). The evolution of friction is dependent both on the slip rate and the gradual evolution of the slipping surfaces (Equation 1). In this formulation, the stability of fault motion depends upon two parameters: (a) the velocity dependence of friction (i.e., the sign of (a-b)) and (b) the capacity of the surrounding medium to store elastic energy compared to the rate of fault weakening with slip. This second criterion is often associated with the difference between the loading stiffness (K) and the fault critical stiffness (Dieterich, 1979; Gu et al., 1984; Rice, 1993; Ruina, 1983):

$$K_c = \frac{(b-a)\sigma_n}{D_c}, \tag{3}$$

In summary, within the rate-and-state framework, the stability behavior of fault can be divided into three domains: (a) stable system if (a-b) > 0; (b) conditionally stable if (a-b) < 0 and $K > K_c$; and (c) unstable if (a-b) < 0 and $K < K_c$.

The performed experiments demonstrated that, for all the tested fault sample, (a-b) decreases with shear displacement (Figure 6), and evolves from velocity strengthening to velocity weakening behavior (i.e., transitioning from stable to the conditionally stable conditions). The parameter (a-b) keeps on decreasing with increasing displacement, producing an increase in K_c favoring more unstable conditions (Leeman et al., 2016; Marone, 2019). Additionally, for simulated gouge and bare surfaces having a high wear rate (FS), D_c also decreases with displacement, accentuating the increase of K_c.

On the experiments performed on FS bare surfaces, unstable sliding occurred after 11–15 mm of shear displacement for velocity step experiments, and after 23–25 mm of displacement for constant velocity experiments. At these displacements, the system is velocity weakening (Figure 6c). Therefore, under quasi-static loading, one

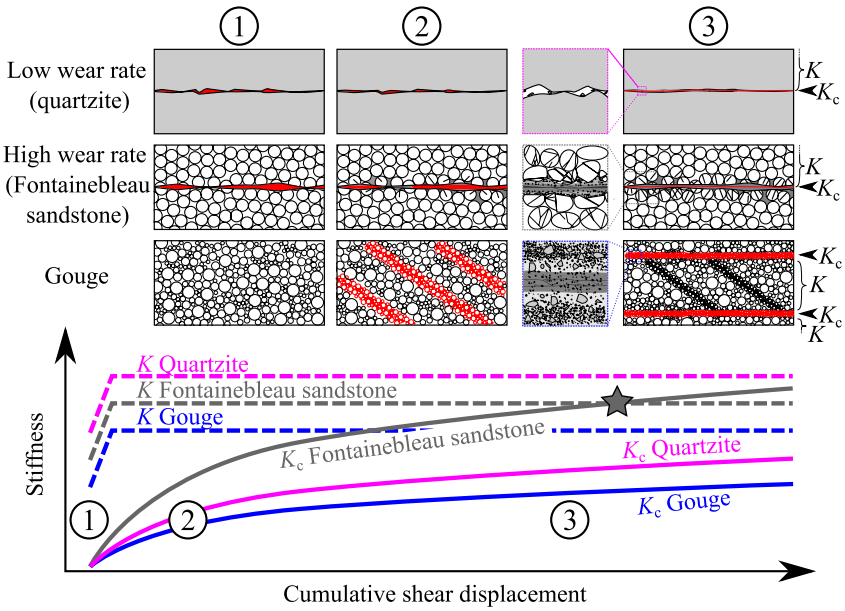

Figure 11. Schematic illustration of fault stability evolution with cumulative shear displacement. The reduction of the stability is directly linked to the increase of shear localization within the fault zone. The drawings represent the evolution of the fault structure at zero (1), intermediate (2) and high cumulative shear displacement (3). Low and high wear rates bare surfaces, as well as simulated gouge are represented. The red area represents the shear zone thickness. The bottom panel represent the comparison between the fault critical stiffness (K_c) and the loading stiffness (K). If K_c reaches similar value as K, instabilities (i.e., stick-slip) spontaneously nucleate. For the tested samples, only Fontainebleau sandstone bare surface reached this state (noted by the star).

would expect that instabilities start nucleating when $K = K_c$ (Gu et al., 1984; Leeman et al., 2016). As mentioned in Section 2.2.3, the effective loading stiffness (apparatus and FS), K, was measured with a dedicated experiment and at the end of each experiment (see Figure S2 in Supporting Information S1). It is found that K is relatively constant from 1 to 17 mm of displacement with an average value of 86.9 ± 1.9 MPa/mm. The K measurements at the end of the constant velocity and velocity step experiments have slightly lower values of 68.7 ± 12.7 MPa/mm. When computing K_c from the rate-and-state parameters inverted from the velocity step experiments we obtained a maximum value of 17.2 MPa/mm. Consequently, for velocity step experiments preformed on FS bare surface, instabilities nucleate under the conditionally stable conditions. We interpret the nucleation of the instability as the result of the frequent velocity steps performed in these experiments allowing to "kick" the system. Indeed, under constant velocity, nucleation arises at much larger displacement (Figures 2 and 3).

5.3. Implications

The experiments performed in this study demonstrate that fault stability largely depends on shear displacement, with strain accumulation and localization as a necessary condition for unstable sliding nucleation. Interestingly, even if the processes promoting localized deformation can be different and depends on the initial fault material (i.e., low or high wear rate bare surface or granular gouge), cumulative shear displacement always leads to a reduction of fault stability (Figures 7 and 8). In all the fault studied, the transition to a more unstable behavior is directly linked to the microstructural evolution of the fault (Figures 10 and 11). In the case of low wear rate bare surfaces, we interpret that the decapitation of the asperities leads to a narrowing of the shear zone (Figure 11 top panels). Therefore, the stability of such faults depends on the wall rock's roughness (e.g., Fryer et al., 2022; Harbord et al., 2017), even if fault roughness seems to not have a first order influence (Beeler, 2023). For high wear rate bare surfaces, the localization of the deformation originates from the rapid wear production and the localization of the deformation along Y-planes following grain size reduction within the produced gouge (Figure 11 central panels). The localization of the deformations here depends on the width (or volume) involved in the deformation, and thus on the grain size within the shear zones. For gouge samples, the localization of the deformation first arises from the development of Riedel shear plans that connect to form boundary or Y-shear

plans (Figure 11 bottom panels). Here again, the localization of the deformation depends on the volume involved in the shear deformations. For all the faults, the localization of the deformation is accompanied by an increase of the fault critical stiffness, K_c (Figure 11 and Figure S6 in Supporting Information S1). The critical stiffness is to be compared with the loading stiffness K, that is, of the fault-surrounding rock, to infer the system stability. For spontaneous instability (i.e., stick-slip) nucleation, K_c must reach value equivalent to K. For the tested fault system, only FS bare surface samples reach this state, whereas for quartzite and simulated gouge K_c is always lower than K (Figure 11).

In addition to the stability transition with increasing shear displacement, faults have been shown to have a stability transition with sliding velocity (e.g., Guérin-Marthe et al., 2019; Kato et al., 1992; Leeman et al., 2018; Marone, 1998a; Mclaskey & Yamashita, 2017; Xu et al., 2018), normal stress (e.g., Bedford & Faulkner, 2021; Chambon & Rudnicki, 2001; Dieterich & Linker, 1992; Giorgetti & Violay, 2021; He et al., 1998; Leeman et al., 2018), temperature (e.g., Blanpied et al., 1998), fluid pressure changes (e.g., Noël, Passelègue, et al., 2019; Scuderi et al., 2017), fault heterogeneity (e.g., Bedford et al., 2022), roughness (e.g., Fryer et al., 2022; Harbord et al., 2017), fabric evolution (e.g., Pozzi et al., 2022), etc. This study, as well as several others, demonstrates that the stability parameters (a-b) and D_c, derived from the rate-and-state friction laws are not material (or interface) properties. Rather, these parameters evolve (in a large range) depending on the fault sliding history (i.e., shear displacement, shear localization, presence of gouge, etc.) and boundary conditions (i.e., sliding velocity, stress, temperature, etc.). This implies that the stability of natural fault segments is not constant but evolves in time and space. Indeed, the performed experiments suggest that a creeping fault patch (i.e., stable sliding patch) may transition to unstable sliding, and nucleate an earthquake, if it accumulates enough shear displacement. Depending on the fault environment and history (i.e., cumulative displacement, shear localization, presence or absence of gouge, etc.), shear displacement as small as few millimeters can be enough for the fault to transition from creep to dynamic instability.

6. Conclusion

We conducted 12 biaxial experiments at 20 MPa of normal stress and up to high (>25 mm) shear displacement. Three pure quartz samples were tested: two bare surfaces, having different wear rates, and simulated gouge were used to characterize how shear displacement influences fault stability. The results show that:

1. Unstable sliding requires a certain amount of shear displacement. On faults tested in the laboratory, 5–15 mm is enough to transition to unstable sliding. Once it nucleates, the instability magnitude (i.e., stress drops) depends on the shearing velocity.
2. All of the tested faults transition from velocity strengthening to velocity weakening with increasing shear displacement. Microstructural analyses reveal that this transition is due to the localization of the deformation.
3. For high wear rate materials, as well as for simulated gouge, the critical slip distance, D_c, decreases with increasing shear displacement. However, for low wear rate materials, D_c remains relatively constant at all of the shear displacement tested.
4. The shearing velocity has a small influence on the stability parameters of the tested fault. For bare-surface samples (a-b) slightly increases with the shearing velocity, while for gouge (a-b) decreases with increasing the velocity. For all of the sample tested, larger shearing velocity seems to favor slightly higher D_c.

This study implies that stability of natural fault segments is not constant, and that the rate-and-state stability parameters are not a material property. Shear displacement as small as few millimeters could be enough for a fault to transition from creep to dynamic instability.

Data Availability Statement

Raw data can be found at https://zenodo.org/record/7385944#.Y4iStXbMKUk (https://doi.org/10.5281/zenodo.7385944).

Acknowledgments
This research was funded by European Research Council (ERC) advance Grant 835012 (TECTONIC). C.G. thanks the Marie Skłodowska-Curie Postdoctoral Grant 101065365 (SHEAR). The authors thanks Marie Violay for providing the quartzite samples. The authors thanks Domenico Mannetta for preparing the thin sections. The authors thanks Giovanni Gaglianone for the help with the granulometry analysis. The authors thanks Marco Brandano for making his optical microscope available for use. The authors thank Giacomo Pozzi for his help technical help during microscope analysis. The authors thanks Tania Ruspandini for SEM assistance. C.N. thanks Barnaby Fryer for the discussion and proofreading. The authors thanks the editor Isabelle Manighetti, the associated editor, John Bedford and an anonymous reviewer for their constructive comments that have helped at improving the manuscript. Open Access Funding provided by Universita degli Studi di Roma La Sapienza within the CRUI-CARE Agreement.

References

Anthony, J. L., & Marone, C. (2005). Influence of particle characteristics on granular friction. *Journal of Geophysical Research*, *110*(B8), B08409. https://doi.org/10.1029/2004JB003399

Baumberger, T., Heslot, F., & Perrin, B. (1994). Crossover from creep to inertial motion in friction dynamics. *Nature*, *367*(6463), 544–546. https://doi.org/10.1038/367544a0

Bedford, J. D., & Faulkner, D. R. (2021). The role of grain size and effective normal stress on localization and the frictional stability of simulated quartz gouge. *Geophysical Research Letters*, *48*(7), e2020GL092023. https://doi.org/10.1029/2020GL092023

Bedford, J. D., Faulkner, D. R., & Lapusta, N. (2022). Fault rock heterogeneity can produce fault weakness and reduce fault stability. *Nature Communications*, *13*(326), 326. https://doi.org/10.1038/s41467-022-27998-2

Beeler, N. M. (2023). On the scale-dependence of fault surface roughness. *Journal of Geophysical Research: Solid Earth*, *128*(2), e2022JB024856. https://doi.org/10.1029/2022jb024856

Beeler, N. M., Tullis, T., Junger, J., Kilgore, B., & Goldsby, D. (2014). Laboratory constraints on models of earthquake recurrence. *Journal of Geophysical Research: Solid Earth*, *119*(12), 8770–8791. https://doi.org/10.1002/2014JB011184

Beeler, N. M., Tullis, T. E., Blanpied, M. L., & Weeks, J. D. (1996). Frictional behavior of large displacement experimental faults. *Journal of Geophysical Research*, *101*(B4), 8697–8715. https://doi.org/10.1029/96JB00411

Beeler, N. M., Tullis, T. E., & Weeks, J. D. (1994). The roles of time and displacement in the evolution effect in rock friction. *Geophysical Research Letters*, *21*(18), 1987–1990. https://doi.org/10.1029/94GL01599

Ben-Zion, Y., & Sammis, C. G. (2003). Characterization of fault zones. *Pure and Applied Geophysics*, *160*(3–4), 677–715. https://doi.org/10.1007/PL00012554

Bied, A. E., Sulem, J., & Martineau, F. (2002). Microstructure of shear zones in Fontainebleau sandstone. *International Journal of Rock Mechanics and Mining Sciences*, *39*(7), 917–932. https://doi.org/10.1016/s1365-1609(02)00068-0

Biegel, R. L., Sammis, C. G., & Dieterich, J. H. (1989). The frictional properties of a simulated gouge having a fractal particle distribution. *Journal of Structural Geology*, *11*(7), 827–846. https://doi.org/10.1016/0191-8141(89)90101-6

Blanpied, M. L., Lockner, D. A., & Byedee, D. (1995). Frictional slip of granite at hydrothermal conditions. *Journal of Geophysical Research*, *100*(B7), 13045–13064. https://doi.org/10.1029/95jb00862

Blanpied, M. L., Marone, C. J., Lockner, D. A., Byerlee, J. D., & King, D. P. (1998). Quantitative measure of the variation in fault rheology due to fluid-rock interactions. *Journal of Geophysical Research*, *103*(B5), 9691–9712. https://doi.org/10.1029/98jb00162

Byerlee, J. (1967). Frictional characteristics of granite under high confining pressure. *Journal of Geophysical Research*, *72*(14), 3639–3648. https://doi.org/10.1029/JZ072i014p03639

Carpenter, B. M. M., Scuderi, M. M., Collettini, C., & Marone, C. (2014). Frictional heterogeneities on carbonate-bearing normal faults: Insights from the Monte Maggio fault, Italy. *Journal of Geophysical Research: Solid Earth*, *119*(12), 9062–9076. https://doi.org/10.1002/2014JB011337

Chambon, G., & Rudnicki, J. W. (2001). Effects of normal stress variations on frictional stability of a fluid-infiltrated fault. *Journal of Geophysical Research: Solid Earth*, *106*(B6), 11353–11372. https://doi.org/10.1029/2001JB900002

Collettini, C., Di Stefano, G., Carpenter, B., Scarlato, P., Tesei, T., Mollo, S., et al. (2014). A novel and versatile apparatus for brittle rock deformation. *International Journal of Rock Mechanics and Mining Sciences*, *66*, 114–123. https://doi.org/10.1016/j.ijrmms.2013.12.005

Cornelio, C., Spagnuolo, E., Aretusini, S., Nielsen, S., Passelègue, F., Violay, M., et al. (2022). Determination of parameters characteristic of dynamic weakening mechanisms during seismic faulting in cohesive rocks. *Journal of Geophysical Research: Solid Earth*, *127*(7), e2022JB024356. https://doi.org/10.1029/2022JB024356

Dieterich, J. H. (1972). Time-dependent friction in rocks. *Journal of Geophysical Research*, *77*(20), 3690–3697. https://doi.org/10.1029/JB077i020p03690

Dieterich, J. H. (1978). Time-dependent friction and the mechanics of stick-slip. *Pure and Applied Geophysics*, *116*(4–5), 790–806. https://doi.org/10.1007/BF00876539

Dieterich, J. H. (1979). Modeling of rock friction: 1. Experimental results and constitutive equations. *Journal of Geophysical Research*, *84*(9), 2161–2168. https://doi.org/10.1007/BF00876539

Dieterich, J. H. (1981). Constitutive properties of faults with simulated gouge. In N. L. Carter, M. Friedman, J. M. Logan, & D. W. Stearns (Eds.), *Geophysical monograph series* (pp. 103–120). https://doi.org/10.1029/GM024p0103

Dieterich, J. H., & Conrad, G. (1984). Effect of humidity on time- and velocity-dependent friction in rocks. *Journal of Geophysical Research*, *89*(B6), 4196–4202. https://doi.org/10.1029/jb089ib06p04196

Dieterich, J. H., & Kilgore, B. D. (1994). Direct observation of frictional contacts: New insights for state-dependent properties. *Pure and Applied Geophysics*, *143*(1–3), 283–302. https://doi.org/10.1007/BF00874332

Dieterich, J. H., & Linker, M. F. (1992). Fault stability under conditions of variable normal stress. *Geophysical Research Letters*, *19*(16), 1691–1694. https://doi.org/10.1029/92GL01821

Di Toro, G., Goldsby, D. L., & Tullis, T. E. (2004). Friction falls towards zero in quartz rock as slip velocity approaches seismic rates. *Nature*, *427*(6973), 436–439. https://doi.org/10.1038/nature02249

Di Toro, G., Han, R., Hirose, T., De Paola, N., Nielsen, S., Mizoguchi, K., et al. (2011). Fault lubrication during earthquakes. *Nature*, *471*(7339), 494–498. https://doi.org/10.1038/nature09838

Engelder, J. T., Logan, J. M., & Handin, J. (1975). The sliding characteristics of sandstone on quartz fault-gouge. *Pure and Applied Geophysics*, *113*(1), 69–86. https://doi.org/10.1007/BF01592900

Fryer, B., Giorgetti, C., Passelègue, F., Momeni, S., Lecampion, B., & Violay, M. (2022). The influence of roughness on experimental fault mechanical behavior and associated microseismicity. *Journal of Geophysical Research: Solid Earth*, *127*(8), e2022JB025113. https://doi.org/10.1029/2022JB025113

Giacomel, P., Ruggieri, R., Scuderi, M. M., Spagnuolo, E., Di Toro, G., & Collettini, C. (2021). Frictional properties of basalt experimental faults and implications for volcano-tectonic settings and geo-energy sites. *Tectonophysics*, *811*(April), 228883. https://doi.org/10.1016/j.tecto.2021.228883

Giorgetti, C., & Violay, M. (2021). The influence of loading path on fault reactivation: A laboratory perspective. *Geophysical Research Letters*, *48*(8), e2020GL091466. https://doi.org/10.1029/2020GL091466

Gu, J. C., Rice, J. R., Ruina, A. L., & Tse, S. T. (1984). Slip motion and stability of a single degree of freedom elastic system with rate and state dependent friction. *Journal of the Mechanics and Physics of Solids*, *32*(3), 167–196. https://doi.org/10.1016/0022-5096(84)90007-3

Gu, Y., & Wong, T. (1994). Development of shear localization in simulated quartz gouge: Effect of cumulative slip and gouge particle size. *Pure and Applied Geophysics*, *143*(1–3), 387–423. https://doi.org/10.1007/BF00874336

Guérin-Marthe, S., Nielsen, S., Bird, R., Giani, S., & Di Toro, G. (2019). Earthquake nucleation size: Evidence of loading rate dependence in laboratory faults. *Journal of Geophysical Research: Solid Earth*, *124*(1), 689–708. https://doi.org/10.1029/2018JB016803

Hadizadeh, J., Tullis, T. E., White, J. C., & Konkachbaev, A. I. (2015). Shear localization, velocity weakening behavior, and development of cataclastic foliation in experimental granite gouge. *Journal of Structural Geology*, *71*, 86–99. https://doi.org/10.1016/j.jsg.2014.10.013

Haied, A., & Kondo, D. (1997). Strain localization in Fontainebleau sandstone: Macroscopic and microscopic investigations. *International Journal of Rock Mechanics and Mining Sciences*, *34*(3–4), 161.e1–161.e13. https://doi.org/10.1016/S1365-1609(97)00216-5

Haines, S. H., Kaproth, B., Marone, C., Saffer, D., & Van der Pluijm, B. (2013). Shear zones in clay-rich fault gouge: A laboratory study of fabric development and evolution. *Journal of Structural Geology*, *51*, 206–225. https://doi.org/10.1016/j.jsg.2013.01.002

Harbord, C. W. A., Nielsen, S. B., De Paola, N., & Holdsworth, R. E. (2017). Earthquake nucleation on rough faults. *Geology*, *45*(10), 931–934. https://doi.org/10.1130/G39181.1

He, C., Ma, S., & Huang, J. (1998). Transition between stable sliding and stick-slip due to variation in slip rate under variable normal stress condition. *Geophysical Research Letters*, *25*(17), 3235–3238. https://doi.org/10.1029/98GL02518

He, C., Wong, T., & Beeler, N. M. (2003). Scaling of stress drop with recurrence interval and loading velocity for laboratory-derived fault strength relations. *Journal of Geophysical Research*, *108*(B1), 2037. https://doi.org/10.1029/2002jb001890

Heslot, F., Baumberger, T., Perrin, B., Caroli, B., & Caroli, C. (1994). Creep, stick-slip, and dry-friction dynamics: Experiments and a heuristic model. *Physical Review*, *49*(6), 4973–4988. https://doi.org/10.1103/PhysRevE.49.4973

Hirose, T., Mizoguchi, K., & Shimamoto, T. (2012). Wear processes in rocks at slow to high slip rates. *Journal of Structural Geology*, *38*, 102–116. https://doi.org/10.1016/j.jsg.2011.12.007

Ikari, M. J., Marone, C., & Saffer, D. M. (2011). On the relation between fault strength and frictional stability. *Geology*, *39*(1), 83–86. https://doi.org/10.1130/G31416.1

Kanamori, H., & Allen, C. R. (1986). Earthquake repeat time and average stress drop. In S. Das, J. Boatwright, & C. H. Scholz (Eds.), *Geophysical monograph series; earthquake source mechanics* (Vol. 37). https://doi.org/10.1029/GM037p0227

Karner, S. L., & Marone, C. (2000). Effects of loading rate and normal stress on stress drop and stick-slip recurrence interval. *Geophysical Monograph Series*, *120*, 187–198. https://doi.org/10.1029/GM120p0187

Kato, N., Yamamoto, K., Yamamoto, H., & Hirasawa, T. (1992). Strain-rate effect on frictional strength and the slip nucleation process. *Tectonophysics*, *211*(1–4), 269–282. https://doi.org/10.1016/0040-1951(92)90064-D

Leeman, J. R., Marone, C., & Saffer, D. M. (2018). Frictional mechanics of slow earthquakes. *Journal of Geophysical Research: Solid Earth*, *123*(9), 7931–7949. https://doi.org/10.1029/2018JB015768

Leeman, J. R., Saffer, D. M., Scuderi, M. M., & Marone, C. (2016). Laboratory observations of slow earthquakes and the spectrum of tectonic fault slip modes. *Nature Communications*, *7*(1), 11104. https://doi.org/10.1038/ncomms11104

Logan, J. M., & Rauenzahn, K. A. (1987). Frictional dependence of gouge mixtures of quartz and montmorillonite on velocity, composition and fabric. *Tectonophysics*, *144*(1–3), 87–108. https://doi.org/10.1016/0040-1951(87)90010-2

Mair, K., & Marone, C. (1999). Friction of simulated fault gouge for a wide range of velocities and normal stresses. *Journal of Geophysical Research*, *104*(B12), 22899–28914. https://doi.org/10.1029/1999JB900279

Manighetti, I., Campillo, M., Bouley, S., & Cotton, F. (2007). Earthquake scaling, fault segmentation, and structural maturity. *Earth and Planetary Science Letters*, *253*(3–4), 429–438. https://doi.org/10.1016/j.epsl.2006.11.004

Marone, C. (1998a). The effect of loading rate on static friction and the rate of fault healing during the earthquake cycle. *Nature*, *391*(6662), 69–72. https://doi.org/10.1038/nature34157

Marone, C. (1998b). Laboratory-derived friction laws and their application to seismic faulting. *Annual Review of Earth and Planetary Sciences*, *26*(1), 643–696. https://doi.org/10.1146/annurev.earth.26.1.643

Marone, C. (2019). The spectrum of fault slip modes from elastodynamic rupture to slow earthquakes. In A. Bizzarri, S. Das, & A. Petri (Eds.), *Proceedings of the international school of physique "Enrico Fermi": Mechanics of earthquake faulting* (pp. 81–94).

Marone, C., & Cox, S. J. D. (1994). Scaling of rock friction constitutive parameters: The effects of surface roughness and cumulative offset on friction of gabbro. *Pure and Applied Geophysics*, *143*(1–3), 359–385. https://doi.org/10.1007/BF00874335

Marone, C., Hobbs, B. E., & Ord, A. (1992). Coulomb constitutive laws for friction: Contrasts in frictional behavior for distributed and localized shear. *Pure and Applied Geophysics*, *139*(2), 195–214. https://doi.org/10.1007/BF00876327

Marone, C., & Kilgore, B. (1993). Scaling of the critical slip distance for seismic faulting with shear strain in fault zones. *Nature*, *362*(6421), 618–621. https://doi.org/10.1038/362618a0

Marone, C., Raleigh, C., & Scholz, C. H. (1990). Frictional behavior and constitutive modeling of simulated fault gouge. *Journal of Geophysical Research*, *95*(B5), 7007–7025. https://doi.org/10.1029/JB095iB05p07007

Marone, C., & Saffer, D. (2007). Fault friction and the upper transition from seismic to aseismic faulting. In T. H. Dixon & J. C. Moore (Eds.), *The seismogenic zone of subduction thrust faults* (pp. 346–369). Retrieved from http://www3.geosc.psu.edu/~cjm38/papers_talks/MaroneSafferMarginsCh12.2007.pdf

Marone, C., Vidale, J. E., & Ellsworth, W. L. (1995). Properties of repeating earthquakes. *Geophysical Research Letters*, *22*(22), 3095–3098. https://doi.org/10.1029/95GL03076

Marrett, R., & Allmendinger, R. W. (1990). Kinematic analysis of fault-slip data. *Journal of Structural Geology*, *12*(8), 973–986. https://doi.org/10.1016/0191-8141(90)90093-E

McLaskey, G. C., Thomas, A. M., Glaser, S. D., & Nadeau, R. M. (2012). Fault healing promotes high-frequency earthquakes in laboratory experiments and on natural faults. *Nature*, *491*(7422), 101–104. https://doi.org/10.1038/nature11512

Mclaskey, G. C., & Yamashita, F. (2017). Slow and fast ruptures on a laboratory fault controlled by loading characteristics. *Journal of Geophysical Research: Solid Earth*, *122*(5), 3719–3738. https://doi.org/10.1002/2016JB013681

Noël, C., Passelègue, F. X., Giorgetti, C., & Violay, M. (2019). Fault reactivation during fluid pressure oscillations: Transition from stable to unstable slip. *Journal of Geophysical Research: Solid Earth*, *124*(11), 10940–10953. https://doi.org/10.1029/2019JB018517

Noël, C., Pimienta, L., & Violay, M. (2019). Time-dependent deformations of sandstone during pore fluid pressure oscillations: Implications for natural and induced seismicity. *Journal of Geophysical Research: Solid Earth*, *124*(1), 801–821. https://doi.org/10.1029/2018JB016546

Power, W. L., Tullis, T. E., & Weeks, J. D. (1988). Roughness and wear during brittle faulting. *Journal of Geophysical Research: Solid Earth*, *93*(B12), 15268–15278. https://doi.org/10.1029/JB093iB12p15268

Pozzi, G., Scuderi, M. M., Tinti, E., Nazzari, M., & Collettini, C. (2022). The role of fault rock fabric in the dynamics of laboratory faults. *Journal of Geophysical Research: Solid Earth*, *127*(6), e2021JB023779. https://doi.org/10.1029/2021JB023779

Rabinowicz, E. (1951). The nature of the static and kinetic coefficients of friction. *Journal of Applied Physics*, *22*(11), 1373–1379. https://doi.org/10.1063/1.1699869

Rathbun, A. P., & Marone, C. (2010). Effect of strain localization on frictional behavior of sheared granular materials. *Journal of Geophysical Research*, *115*(B1), B01204. https://doi.org/10.1029/2009jb006466

Reviron, N., Reuschlé, T., & Bernard, J. D. (2009). The brittle deformation regime of water-saturated siliceous sandstones. *Geophysical Journal International*, *178*(3), 1766–1778. https://doi.org/10.1111/j.1365-246X.2009.04236.x

Rice, J. R. (1993). Spatio-temporal complexity of slip on a fault. *Journal of Geophysical Research*, *98*(B6), 9885–9907. https://doi.org/10.1029/93JB00191

Rice, J. R. (2006). Heating and weakening of faults during earthquake slip. *Journal of Geophysical Research*, *111*(5), 1–29. https://doi.org/10.1029/2005JB004006

Ruina, A. (1980). *Friction laws and instabilities: A quasistatic analysis of some dry frictional behavior*. Brown University.

Ruina, A. (1983). Slip instability and state variable friction law. *Journal of Geophysical Research*, *88*(B12), 10359–10370. https://doi.org/10.1029/JB088iB12p10359

Sammis, C. G., & Biegel, R. L. (1989). Fractals, fault-gouge, and friction. *Pure and Applied Geophysics*, *131*(1–2), 255–271. https://doi.org/10.1007/BF00874490

Scholz, C., Molnar, P., & Johnson, T. (1972). Detailed studies of frictional sliding of granite and implications for the earthquake mechanism. *Journal of Geophysical Research*, *77*(32), 6392–6406. https://doi.org/10.1029/JB077i032p06392

Scholz, C. H. (1987). Wear and gouge formation in brittle faulting. *Geology*, *15*(6), 493–495. https://doi.org/10.1130/0091-7613(1987)15<493:WAGFIB>2.0.CO;2

Scholz, C. H. (2019). The mechanics of earthquakes and faulting. In *The mechanics of earthquakes and faulting* (3rd ed.). Cambridge University Press. https://doi.org/10.1017/9781316681473

Schubnel, A., Thompson, B. D., Fortin, J., Guéguen, Y., & Young, R. P. (2007). Fluid-induced rupture experiment on Fontainebleau sandstone: Premonitory activity, rupture propagation, and aftershocks. *Geophysical Research Letters*, *34*(19), L19307. https://doi.org/10.1029/2007GL031076

Scuderi, M. M., Carpenter, B. M., & Marone, C. (2014). Physicochemical processes of frictional healing: Effects of water on stick-slip stress drop and friction of granular fault gouge. *Journal of Geophysical Research: Solid Earth*, *119*(5), 4090–4105. https://doi.org/10.1002/2013JB010641

Scuderi, M. M., Collettini, C., & Marone, C. (2017). Frictional stability and earthquake triggering during fluid pressure stimulation of an experimental fault. *Earth and Planetary Science Letters*, *477*(November), 84–96. https://doi.org/10.1016/j.epsl.2017.08.009

Scuderi, M. M., Collettini, C., Viti, C., Tinti, E., & Marone, C. (2017). Evolution of shear fabric in granular fault gouge from stable sliding to stick slip and implications for fault slip mode. *Geology*, *45*(8), 731–734. https://doi.org/10.1130/G39033.1

Sibson, R. H. (1977). Fault rocks and fault mechanisms. *Journal of the Geological Society*, *133*(3), 191–213. https://doi.org/10.1144/gsjgs.133.3.0191

Sibson, R. H. (1986). Brecciation processes in fault zones: Inferences from earthquake rupturing. *Pure and Applied Geophysics*, *124*(1–2), 159–175. https://doi.org/10.1007/BF00875724

Skarbek, R. M., & Savage, H. M. (2019). RSFit3000: A MATLAB GUI-based program for determining rate and state frictional parameters from experimental data. *Geosphere*, *15*(5), 1665–1676. https://doi.org/10.1130/GES02122.1

Sulem, J., & Ouffroukh, H. (2006). Hydromechanical behaviour of Fontainebleau sandstone. *Rock Mechanics and Rock Engineering*, *39*(3), 185–213. https://doi.org/10.1007/s00603-005-0065-4

Tesei, T., Carpenter, B. M., Giorgetti, C., Scuderi, M. M., Sagy, A., Scarlato, P., & Collettini, C. (2017). Friction and scale-dependent deformation processes of large experimental carbonate faults. *Journal of Structural Geology*, *100*, 12–23. https://doi.org/10.1016/j.jsg.2017.05.008

Tesei, T., Collettini, C., Barchi, M. R., Carpenter, B. M., & Di Stefano, G. (2014). Heterogeneous strength and fault zone complexity of carbonate-bearing thrusts with possible implications for seismicity. *Earth and Planetary Science Letters*, *408*, 307–318. https://doi.org/10.1016/j.epsl.2014.10.021

Tullis, T. E., & Weeks, J. D. (1986). Constitutive behavior and stability of frictional sliding of granite. *Pure and Applied Geophysics*, *124*(3), 383–414. https://doi.org/10.1007/BF00877209

Wong, T., Gu, Y., Yanagidani, T., & Zhao, Y. (1992). Stabilization of faulting by cumulative slip. In *Fault mechanics and transport properties of rocks* (pp. 119–143). https://doi.org/10.1016/S0074-6142(08)62820-X

Wong, T.-F., & Zhao, Y. (1990). Effects of load point velocity on frictional instability behavior. *Tectonophysics*, *175*(1–3), 177–195. https://doi.org/10.1016/0040-1951(90)90137-W

Xu, S., Fukuyama, E., Yamashita, F., Mizoguchi, K., Takizawa, S., & Kawakata, H. (2018). Strain rate effect on fault slip and rupture evolution: Insight from meter-scale rock friction experiments. *Tectonophysics*, *733*, 209–231. https://doi.org/10.1016/j.tecto.2017.11.039

References From the Supporting Information

Bourbié, T., & Zinszner, B. (1985). Hydraulic and acoustic properties as a function of porosity in Fontainebleau Sandstone. *Journal of Geophysical Research*, *90*(B13), 11524. https://doi.org/10.1029/JB090iB13p11524

Fabre, D., & Gustkiewicz, J. (1997). Poroelastic properties of limestones and sandstones under hydrostatic conditions. *International Journal of Rock Mechanics and Mining Sciences*, *34*(1), 127–134. https://doi.org/10.1016/S0148-9062(96)00037-X

Fredrich, J. T., Greaves, K. H., & Martin, J. W. (1993). Pore geometry and transport properties of Fontainebleau sandstone. *International Journal of Rock Mechanics and Mining Sciences*, *30*(7), 691–697. https://doi.org/10.1016/0148-9062(93)90007-Z

Noël, C., Baud, P., & Violay, M. (2021). Effect of water on sandstone's fracture toughness and frictional parameters: Brittle strength constraints. *International Journal of Rock Mechanics and Mining Sciences*, *147*, 104916. https://doi.org/10.1016/j.ijrmms.2021.104916

Pimienta, L., Fortin, J., & Guéguen, Y. (2015a). Bulk modulus dispersion and attenuation in sandstones. *Geophysics*, *80*(2), D111–D127. https://doi.org/10.1190/geo2014-0335.1

Pimienta, L., Fortin, J., & Guéguen, Y. (2015b). Experimental study of young's modulus dispersion and attenuation in fully saturated sandstones. *Geophysics*, *80*(5), L57–L72. https://doi.org/10.1190/geo2014-0532.1